PERSPECTIVE

Check for updates

Nanostructured mixed transition metal oxide spinels for supercapacitor applications

Sasanka Deka (ID)

There have been numerous applications of supercapacitors in day-to-day life. Along with batteries and fuel cells, supercapacitors play an essential role in supplementary electrochemical energy storage technologies. They are used as power sources in portable electronics, automobiles, power backup, medical equipment, *etc*. Among various working electrode materials explored for supercapacitors, nanostructured transition metal oxides containing mixed metals are highly specific and special, because of their stability, variable oxidation states of the constituted metal ions, possibility to tune the mixed metal combinations, and existence of new battery types and extrinsic pseudocapacitance. This review presents the key features and recent developments in the direction of synthesis and electrochemical energy storage behavior of some of the recent morphology-oriented transition metal oxide and mixed transition metal oxide nanoparticles. We also targeted the studies on a few of the recently developed flexible and bendable supercapacitor devices based on these mixed transition metal oxides.

1. Introduction

An electrochemical energy storage (EES) or charge storage system refers to the system of converting electrical energy from grids into a form that can be stored for converting back to electrical energy when required. Electrochemical supercapacitors (SCs) are a type of high efficiency and potential rechargeable EES system that have drawn tremendous attention in the past few years owing to their fast charging/discharging capability (fast redox reaction kinetics), high capacity, high power and energy densities and long cycle life.[1,2] Compared to commercial batteries, SCs are becoming most promising EES systems as here too the electrical and chemical energies share the same carrier, the 'electron'.[3,4] SCs have shown high credibility in the field of lightweight portable electronic equipment and hybrid power cars.[5] In general, SCs are divided into three types, *viz*. electrical double-layer capacitors (EDLCs), pseudocapacitors (PCs) and the asymmetric combination of both EDLCs and PCs that results in hybrid capacitors (HCs).[2,6] In EDLCs, the energy is stored by the accumulation of charges across the electrode–electrolyte interface and results in the formation of a Helmholtz double layer. In PCs, the energy storage processes occur through rapid and reversible faradaic redox reactions.[7,8] The PCs show capacitive performance due to the ultrafast reversible redox reaction occurring across the electrode/electrolyte interface and not due to the electrostatic inter-

actions. The electrolyte behavior and interaction with the electrode materials have a significant impact on pseudocapacitive behavior and consequently pseudocapacitance. Apart from these three types of SCs, two more types of SCs are discussed nowadays. Even though it is difficult to classify them as new types of SCs, the electrode materials are newly classified as (a) battery-type SCs and/or (b) extrinsic pseudocapacitors.[9,10] In extrinsic PCs, the surface-controlled process is more dominant compared to the diffusive-controlled contribution. This behavior is mainly seen in nanomaterials, where the bulk phase behaves as a battery material; however, an increase in the surface area and pseudocapacitive behavior emerges due to the size reduction to the nanometer size. In battery-type SCs, the diffusive controlled contribution dominates over the surface-controlled process. They follow the intercalation–deintercalation mechanism inside the bulk phase of the host materials.

With the rapid advancement in the field of nanoscience and nanotechnology, the electrochemical performances of supercapacitors have been significantly improved. This is attributed to the electrode's high surface area for storing charges and the ease with which the electrolyte diffuses into the nanostructured electrodes. However, the current obstruction in the performance of SCs is their low energy density and it still remains a bottleneck.[11] It is known that the energy density of a SC relies on both capacitance and applied potential values. The energy density of a SC can be tuned by increasing the operating potential window and capacitance value of the electrode material.[12] Therefore, it is highly desired to develop an electrode material which can show excellent energy storage performance.

Department of Chemistry, University of Delhi, North Campus, Delhi 110007, India.
E-mail: sdeka@chemistry.du.ac.in

There are various types of electrode materials explored to date, *e.g.* carbon materials, conductive polymers, transition metal oxides (TMOs), transition metal chalcogenides, transition metal borons, layered double hydroxides (LDHs), MXenes, *etc.* Carbon materials like activated carbon (AC),[13,14] graphene,[15] carbon nanofibers,[16] carbon nanotubes (CNTs),[17] and g-C$_3$N$_4$[18] have a high surface area, high porosity, good electrical conductivity and chemical stability in different types of electrolytes, and they offer EDLC behavior. Although they have been widely studied, their overall performance is limited, owing to their low specific capacitance (C_{SP}), high cost and low energy density.[19] Due to these shortcomings, the use of carbon-based electrode materials is limited for real-life applications.[20] Similarly, conductive polymers exhibit good pseudocapacitive performances but they have low stability and get easily detached from the substrate.[21,22] Transition metal sulphide based supercapacitors are not highly stable in aqueous electrolyte medium and are prone to get oxidized.[23] Also, transition metal boranes show good pseudocapacitive performance[24] but they show low rate capability and are not operable under high temperature conditions.[25]

Transition metal oxides are highly stable materials and have higher specific capacitance along with high energy density, and are found to be suitable against the above-mentioned lacunae associated with other materials. RuO$_2$ was the first state-of-the-art TMO material which was examined for energy storage applications and showed excellent pseudocapacitive performance.[26,27] However, the high cost and toxic nature of RuO$_2$ limited its application in the field of supercapacitors. Thereafter, non-noble transition metal oxides like NiO, Co$_3$O$_4$, ZnO and MnO$_2$ were thought to be better alternatives due to their high natural abundance and appreciable energy storage performance. Some other developments in this area include blending of TMOs with metal–organic-framework (MOF) compounds to increase the porosity, electrical conductivity and chemical stability of the composites,[28] introduction of layered nanoclay and layered nanoclay-based electrodes,[29] and so on. Yet, they also exhibit poor electrical conductivity; so to overcome these issues, mixed transition metal oxides (MTMOs) came into existence. MTMOs have gained significant attention in recent times in the field of SCs. MTMOs due to the presence of two or more metal ions with variable oxidation states show synergistic effects. The nonlinear cumulative effects of two metal cations combined with comparable or related results of their various activities, or with subsequent or supplemental activities, are what are being referred to as the synergistic effects in this instance. Due to these synergistic effects, MTMOs show increased electrical conductivity, enriched redox-active sites and better electrochemical performance than normal TMOs and other electrode materials. Among different MTMOs, spinels are the mostly studied electrode materials for SC applications because of their exotic properties, such as enhanced electrochemical activity, low resistance, compatibility with a wide range of electrolytes, low cost, good chemical durability in long cycling, and environmental friendliness. Co$_3$O$_4$, Mn$_3$O$_4$, NiCo$_2$O$_4$, MnCo$_2$O$_4$, ZnCo$_2$O$_4$, CuCo$_2$O$_4$, *etc.* are a few examples which exhibit extraordinary properties like high specific capacitance, low cost, high chemical stability and non-toxic nature.

In this review article, we will be focusing mainly on spinel based MTMO nanostructured electrode materials for SC applications. There are plenty of review articles available on basic SC properties, applications (coin cells and flexible devices), and different types of electrode materials including LDHs, TMOs, MXenes, carbon, graphene, *etc.*, without giving much emphasis on MTMO spinels. Therefore, we found the necessity of a review article solely based on mixed transition metal oxide spinels for SC applications. The materials considered and reasons behind these considerations and types of SCs discussed in this review are summarized in Fig. 1. The various strategies for the improvement in the energy storage performance of MTMO spinel electrode materials and their electrochemical charge storage properties are elaborated in detail in this review article.

2. Transition metal oxides

The excellent pseudocapacitive performance of TMOs is mainly due to the variable oxidation states caused by the incomplete d-subshell. These characteristic properties lead to unique structural, electrical and electrochemical charge storage properties. Compared to their bulk counterparts, TMO nanoparticles (NPs) exhibit a high surface area along with a high surface-to-volume ratio and a porous structure encouraging the efficient use of TMOs in energy storage applications. In summary, TMOs must exhibit a few basic properties for energy storage which are as follows: (a) high electrical conductivity, (b) variable oxidation states with no observed change in the phase over a wide potential range, and (3) rapid redox reactions due to the switching of ions within the interlayers of the
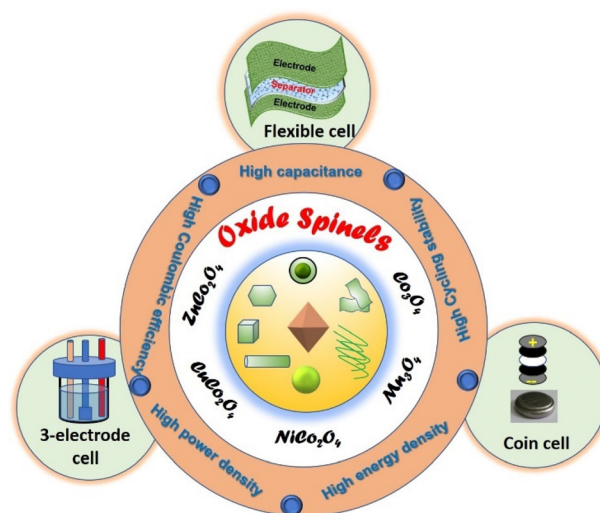

Fig. 1 Schematic illustration of the TMOs considered in this review and their SC studies.

material.[30] Until now, various TMOs with different morphologies and composites have been explored for supercapacitor applications by researchers which include RuO_2, MnO_2, Co_3O_4, Mn_3O_4, Fe_2O_3, Fe_3O_4, V_2O_5, NiO, and many more.[31]

3. Transition metal oxide spinels

'Spinels' belong to a wide family of minerals having a general formula AB_2X_4 where A is a divalent cation like Mg, Mn, Fe, Co, Ni, Cu, Zn, *etc.*, B is a trivalent cation like Al, Mn, Fe, Co, Ni, *etc.* and X is either oxygen or sulphur. When X is sulphur, the spinels are known as thiospinels, *e.g.* $CuCo_2S_4$, Co_3S_4, *etc.*[32,33] Oxide spinels or transition metal oxide spinels are a class of TMOs with varieties of magnetic, electrical, magneto-optic and opto-electronic properties.[34] The spinel structures can be further divided into two types: (a) normal spinels and (b) inverse spinels. Normal spinels are represented as $(A^{II})^{tet}(B^{III})_2^{oct}O_4$ in which the A^{II} cations occupy $1/8^{th}$ of tetrahedral voids whereas the trivalent B^{III} cations occupy half (1/2) of octahedral voids. $MgAl_2O_4$, $ZnFe_2O_4$, Co_3O_4, *etc.* are a few examples of normal spinels. Inverse spinels are represented as $(B^{III})^{tet}(A^{II})^{oct}(B^{III})^{oct}O_4$ where the A^{II} ions occupy $1/4^{th}$ of the octahedral voids, whereas one-half of B^{III} ions occupy $1/8^{th}$ of the tetrahedral voids, and the other half occupy $1/4^{th}$ of the octahedral sites. Fe_3O_4, $CoFe_2O_4$, $NiCo_2O_4$, $NiFe_2O_4$, *etc.*, are a few examples that have inverse spinel structure. The spinel structures are too affected by the crystal-field stabilization energy (CFSE) values of metal ions and the methods of preparation in bottom-up approaches. When the CFSE value of B^{III} is more than that of A^{II} ions at an octahedral site, it attains a normal spinel structure; however, when the CFSE value of A^{II} ions is more than that of B^{III} ions at an octahedral site, we observe an inverse spinel structure. Fig. 2 shows the crystal structure difference of normal and inverse spinels.[35] Studies show that transition metal oxide spinels are one of the potential candidates for SC applications. There are many factors that make the TMO spinels more advantageous than their counter-

parts. Excellent physico–chemical properties, such as captivating electrical conductivity, stability in harsh electrochemical systems and low charge transfer resistance of TMO spinels are prominent.[35,36] Another speciality of TMO spinels is their potential to attain high capacitance at low cost. However, the best part of TMOs as potent electrode materials in SCs is the multioxidation states of the constituent metals. Even though by definition cation A is divalent and cation B is trivalent in spinels, the possibility of having both $A^{II/III}$ and $B^{II/III/IV}$ depending on the synthesis conditions made[34,37] the TMO spinels excellent for electrochemical redox reactions and charge storage.

3.1. Simple TMO spinels

3.1.1. Co_3O_4 nanostructures. Before exploring the mixed metal oxide spinels for SCs, here we first tried to learn the EES properties of two simple TMO spinels, *i.e.* Co_3O_4 and Mn_3O_4 normal spinels. The acquired knowledge from this species will help us to understand better the MTMO spinel system for SC applications. Along with RuO_2, Co_3O_4 was a great choice for SCs at the beginning because of the possible multioxidation states of cobalt(II,III,IV) in Co_3O_4 similar to MTMO and its perfect pseudocapacitance. Co_3O_4 based NPs are an attractive class of materials which show redox reactions when they come into contact with the electrolyte (KOH, NaOH) as described below:

$$Co_3O_4 + OH^- \leftrightarrow 3CoOOH^- + e^- \quad (1)$$

$$CoOOH^- + OH^- \leftrightarrow CoO_2 + H_2O + e^- \quad (2)$$
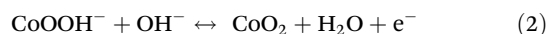
Because of their relatively high theoretical specific capacitance (3650 F g^{-1}), outstanding electrical conductance with good chemical and thermal durability, they are considered as a potential active material.[38,39] The hydrothermal synthesis process is commonly used to develop nanostructured Co_3O_4 materials. This synthesis method is easy to perform at low cost and the size, shape, crystal structure of nanomaterials can be easily controlled by conducting the reactions at lower temperatures.[40] As an example, Xia *et al.*[41] used a straightforward hydrothermal approach for inducing a large area growth of self-supporting Co_3O_4 hollow nanowire arrays. These nanowire arrays have a rough texture consisting of ring structures with a hollow interior. A β-$Co(OH)_2$ intermediate with (001) orientation played an important role in obtaining the hollow nanowire structure of Co_3O_4. The high specific capacitance and rate capability (599 F g^{-1} at 2 A g^{-1} and 439 F g^{-1} at 40 A g^{-1}) of this self-supporting hollow Co_3O_4 nanowire array in 1.0 M KOH were attributed to the roughness, high surface area, and the porosity between individual nanowires which facilitates electrolyte penetration within the arrays. Another good rate capability and cycling stability material was single-crystalline Co_3O_4 nanowire arrays grown over Ni-foam.[42] These nanoarrays were sharply pointed with an average diameter of ~70 nm with the length of the arrays being ~25 μm. The as-produced mono-crystal-Co_3O_4 nanowire arrays exhibited impressive pseudocapacitor capability, with a high capacitance of 610 F g^{-1} at 40 A
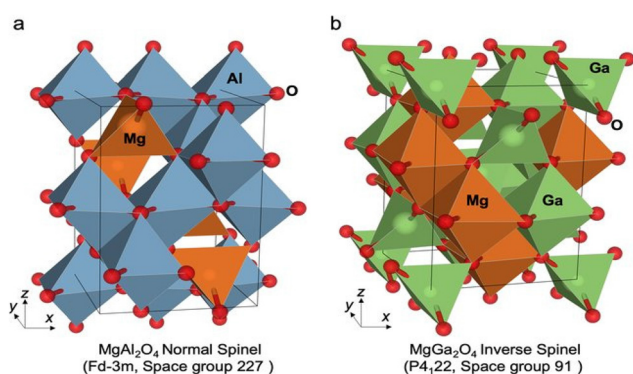

Fig. 2 Schematic representation of the face centred cubic (fcc) crystal structure of a (a) normal spinel and (b) inverse spinel (Reproduced from ref. 35 with permission from Springer Nature, copyright 2020).

g^{-1} and 754 F g^{-1} at 2 A g^{-1}. Here, the observed performance of the nanoarrays was ascribed to their unique 1-dimensional (1D) porous nanostructure which promotes rapid redox reactions at the electrode/electrolyte interface. Moreover, the high surface area and open geometry between the nanowires delivered more active sites and allowed easier electrolyte penetration into the inner region of the electrode.

1-Dimensional (1D) Co_3O_4 hollow nanostructures were prepared via a controlled thermolysis precursor method, where Co $(CH_3COO)_2$ ethanol solution was re-crystallized to produce 1D hollow nanostructures, which were then transformed into Co_3O_4 boxes via the Kirkendall effect. This material possessed a hollow box-like structure with a consistent length, width, and height and a polycrystalline SAED pattern (Fig. 3a).[43] These Co_3O_4 boxes have higher specific capacitance and capacitance retention compared to commercial Co_3O_4 powders with the same specific surface area (Fig. 3b). The high specific capacitance was attributed to their hollow structure with broken ends and high roughness as revealed by the SEM images. The high roughness also indicated that boxes might be composed of Co_3O_4 NPs. For the production of well-defined hierarchical Co_3O_4 hollow nanocubes with consistent porous architectures, Zhao et al. employed a Cu_2O template-assisted method with a post-calcination process in air.[44] Fig. 3d shows the hollow internal features of Co_3O_4 nanostructures. It is worth noting that the morphology and dimensions of $Co(OH)_2$ precursors were well inherited by Co_3O_4 hollow nanocubes with nanosheet thicknesses of roughly 5 nm. The galvanostatic charge–discharge (GCD) curve derived from the specific capaci-

tance of the Co_3O_4 electrode was found to be 404.9 F g^{-1} at a current density of 0.5 A g^{-1} (Fig. 3e) and indicated a strong rate capability and cycling stability at 20 A g^{-1}. However, the electrode can retain 95% capacitance up to 2000 cycles only possibly due to the structural deterioration of the Co_3O_4 materials.[44] The high electrochemical performance is attributed to both nanosheet networks and porous interconnections within the hollow nanocube structure promoting faster electrolyte ion transportation. These results summarize that Co_3O_4 nanomaterials with different morphological modifications could be attractive for supercapacitor applications.[43,44] Moreover, in comparison, the CV curve shape of Co_3O_4 nanomaterials is totally different from those of EDLCs (which have an almost rectangular shape), which reveals that the capacitance characteristics of Co_3O_4 are those of typical pseudocapacitive capacitance (Fig. 3c) and corroborating redox eqn (1) and (2).[45]

Furthermore, a $NiMoO_4@Co_3O_4$/carbon aerogel ternary composite based asymmetric supercapacitor (ASC) device was fabricated, which exhibited a large capacitance of 125.4 F g^{-1} at 0.5 A g^{-1} (Fig. 3f). The performance of this device is attributed to the synergistic effect of the good conduction capability of the porous 3D structure derived from the carbon aerogel and the large specific capacitance contributed by the transition metal oxides.[46]

Shape controlled Co_3O_4 (nanorods, nanocubes, nanosheets, hierarchical, etc.) were studied using various approaches which displayed potential SC properties and performances due to the aforementioned Co^{II}–Co^{III}–Co^{IV} interactions, high surface area
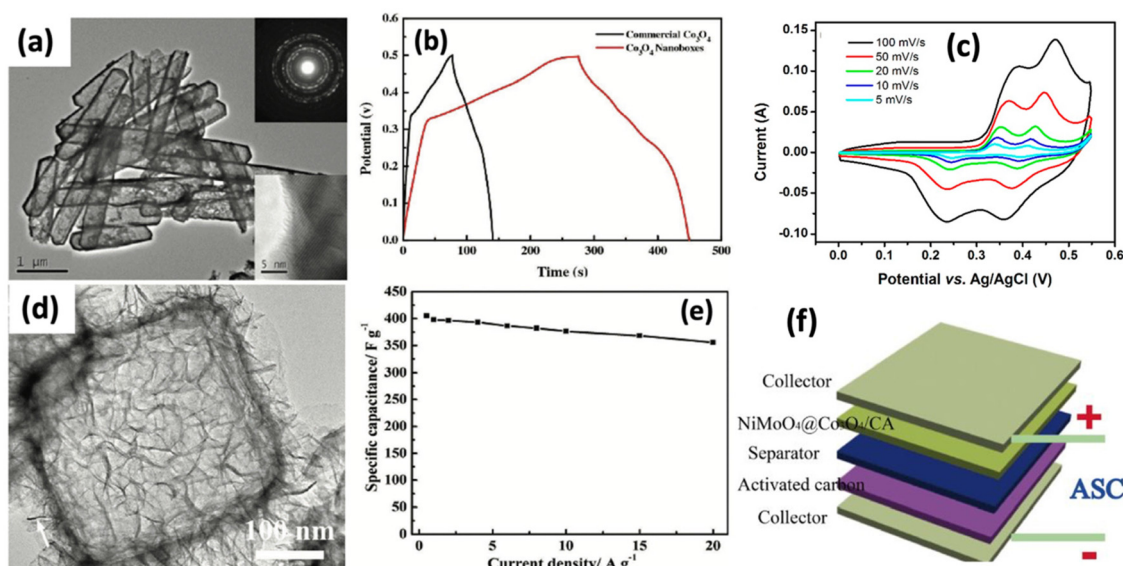

Fig. 3 (a) The TEM images of Co_3O_4 boxes taken after annealing the precursor prisms. The inset shows the HR-TEM image and the SAED pattern of Co_3O_4 and (b) GCD curves of Co_3O_4 boxes and commercial Co_3O_4 at the same current density of 0.5 A g^{-1} (Reproduced from ref. 43 with permission from Elsevier, copyright 2013). (c) CV of porous thin-wall hollow Co_3O_4 spheres (Reproduced from ref. 45 with permission from MDPI, copyright 2019). (d) The TEM image shows the hierarchical morphology of Co_3O_4 hollow nanocubes and (e) capacitance retention curve of the hierarchical Co_3O_4 hollow nanocubes at various current densities (Reproduced from ref. 44 with permission from Elsevier, copyright 2015). (f) Schematic illustration of the $NiMoO_4@Co_3O_4$/carbon aerogel ternary composite ASC device (Reproduced from ref. 46 with permission from Hindawi, copyright 2020).

and porosity, better contact across the electrode/electrolyte interface and faster ion transport.[47–51] Deori *et al.* developed a simple solvothermal strategy to synthesize highly stable, pure phased Co_3O_4 NPs with controlled size and morphologies *viz.*, nanocubes, hexagonal platelets and nanospheres from a Co $(CH_3COO)_2 \cdot 4H_2O$ precursor in ethanol solvent at 220 °C (Fig. 4a–d).[40] The hexagonal platelets' multilayer structural arrangement and the existence of extraordinarily high numbers of regularly ordered pores lead to the improved electrochemical characteristics of Co_3O_4. The increment in the current density (0.5 to 2.5 A g^{-1}) slows down the reaction time between the electrode and electrolyte surface and therefore a decrement in the specific capacitance from 476 F g^{-1} to 150 F g^{-1} was observed (Fig. 4e and f).[52] The spinel cobalt oxide electrode also delivered a higher energy density (42.3 W h kg^{-1}) and power density (6.4 kW kg^{-1}) and long cycling stability. Thereafter, hexagonal Co_3O_4 nanoplatelets were explored for SC applications due to their high porosity, surface area and redox behavior.[53,54] Recently, reduced graphene oxide (RGO) was incorporated into metal–organic framework (MOF)-derived Co_3O_4 hexagons to achieve high EES performance by full utilization of the integrated porous layered architectures.[55] A Co_3O_4 nanocube@Co-MOF composite was prepared *via* a controllable and facile one-pot hydrothermal method under highly alkaline conditions. The solid-state flexible device made from this composite provided space for the electrochemical reaction, intercalation/de-intercalation of K^+ (from the KOH electrolyte) during

the energy storage process and alkaline stability to increase redox active sites.[56] A reflux condensation mediated deposition method was used to deposit Co_3O_4 nanosheets on $ZnFe_2O_4$ nanoflakes.[57] Here, $ZnFe_2O_4$ nanoflake arrays were first synthesized on a stainless-steel mess substrate, and then Co_3O_4 nanosheets were deposited on these nanoflakes at 90 °C in the presence of urea and ammonium fluoride. Nanocage morphology is another example to fully utilize the pores in Co_3O_4.[58] Further emphases have been given on synthesis methods, rationally designing the material structure, and evolution of morphology in other Co_3O_4 EES studies including the annealing of electrode materials.[59,60]

3.1.2. Mn_3O_4 nanostructures.

Apart from Co_3O_4, Mn_3O_4 (Hausmannite) has also been considered as a potential material for SC applications. Due to its distinctive characteristics, including its high theoretical capacitance (1370 F g^{-1}), changeable oxidation states, pronounced Jahn–Teller effect, large potential window, environmental friendliness, and affordability, Mn_3O_4 has received a lot of attention as an electrode material. The specific capacitance of the material specifically depends on the morphology, electrical conductivity and mass loadings. Various morphologies exhibit different surface areas, surface to volume ratios and porosities.[61] Different synthetic approaches such as hydrothermal, solvothermal, chemical precipitation, cathodic electrodeposition *etc.* have been used to develop different morphologies of Mn_3O_4 like 1D (nanorods), 2D (nanoplates) and 3D (nanocubes, nanoflowers,
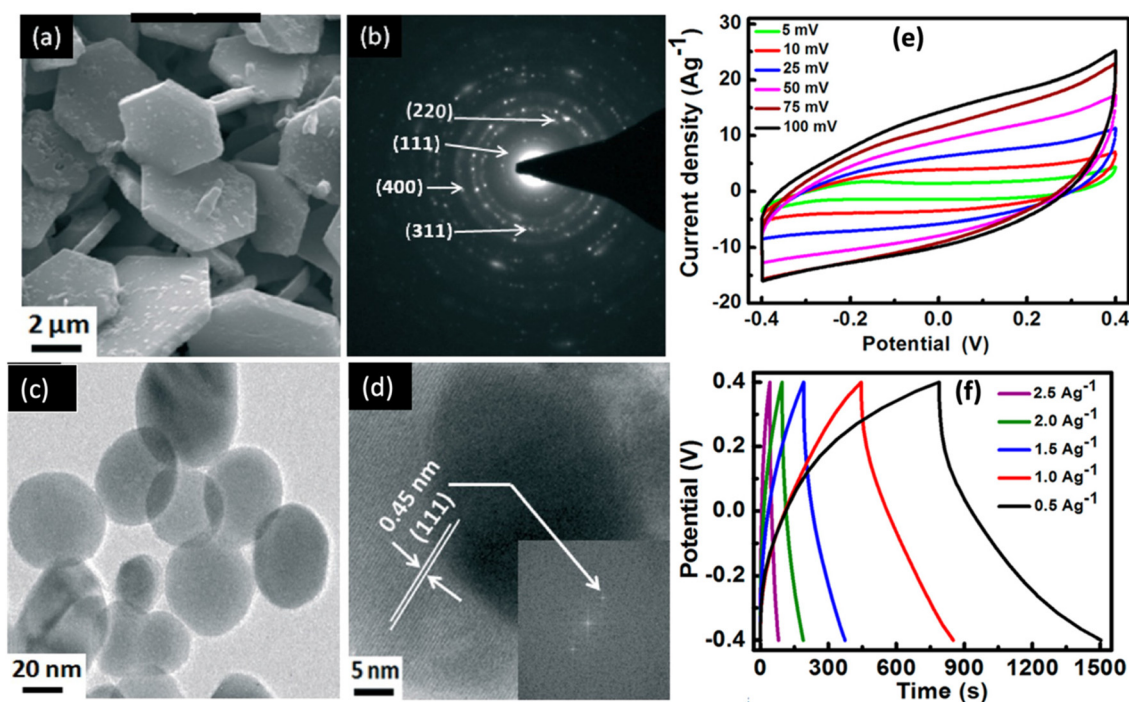

Fig. 4 (a) SEM images of hexagonal Co_3O_4 nanoplatelets and (b) TEM-SAED pattern. (c) Low magnification TEM image and (d) representative phase contrast HRTEM image of a single sample spherical Co_3O_4 NP (Reproduced from ref. 40 with permission from the Royal Society of Chemistry, copyright 2013). (e) CV curves at different scan rates and (f) GCD curves at different current densities of the as-synthesized Co_3O_4 hexagonal nanoplatelets (Reproduced from ref. 52 with permission from American Chemical Society, copyright 2019).

nano-octahedra and nanospheres).[62–64] For *e.g.*, vertically aligned Mn_3O_4 nanorods prepared *via* a one-step cathodic electrodeposition of manganese oxide from chloride exhibited excellent capacitive behavior with a specific capacitance of 321 F g^{-1} at a scan rate of 2 mV s^{-1} and a long cycling stability of 91.7% after 1000 charge–discharge cycles.[62] Similarly, various electrochemical studies have been conducted for this material but it shows poor conductivity and a change in volume during the insertion and de-insertion of electrolyte ions.

To overcome these challenges, Mn_3O_4 NPs was supported with a carbonaceous material or doping with hetero-atoms in many ways to achieve a high specific capacitance and a high retention rate to gain better cycling stability for particular charging–discharging cycles. The synergistic effect dominates here which increases the material supercapacitor performance through the support of carbonous materials or doping of hetero-atoms.[61] An electrostatic heterocoagulation process was used for effective mixing of Mn_3O_4 and carbon nanotubes which facilitated enhanced capacitive behavior with a high specific capacitance (2.8 F cm^{-2}) and a capacitance retention of 88% in the scan range of 2–100 mV s^{-1}.[65] These results showed that the composite materials can be better substitutes for practical applications in electrochemical supercapacitors. Many of the reported Mn_3O_4 materials have rich voids and gaps in the structure, and abundant pseudocapacitive sites, which offer good cycling stability and modifiability.[66]

Although the literature on Co_3O_4 and Mn_3O_4 is pretty much rich, their electrochemical performance is still hindered by low specific surface areas, low cycling stability and most importantly fewer active sites. According to literature reports, these simple TMO spinel nanostructures can be mixed with carbon compounds such as graphene, carbon nanotubes, porous carbon, and other carbon materials to create high surface areas and effective electrode materials. Table 1 compares some of the best EES properties of nanostructured Co_3O_4 and Mn_3O_4 electrode materials. However, as mentioned, the lacunae faced by these materials could be well addressed by the development of MTMO spinels. Due to their (mixed metal ions) synergistic effects the electrochemical performances were notably enhanced, which are discussed in the next sections.

3.2. Mixed transition metal oxide spinels for supercapacitor applications

MTMOs have gained significant attention as a sought-after energy-storage material. This is due to mixed transition metal oxides' unique features, which include variable multiple oxidation states of constituted mixed metals that provide excellent pseudocapacitance activity, the ability to intercalate ions and electrons into the MTMO lattice, and their intrinsic high stability.[88] Nanostructured MTMOs (*e.g.* $CuCo_2O_4$, $ZnCo_2O_4$, and $NiCo_2O_4$ *etc.*) have gained significant attention as working electrode materials since they deliver rich redox activity and high surface area which provide exposed storage surface sites and the multiple oxidation states of metal ions that allow efficient faradaic reactions. Furthermore, thin/flexible electrodes with good mechanical and chemical stability can also be integrated

Table 1 Comparison of the electrochemical performances of simple TMO spinel materials

Sl. no.	Electrode material	C_{SP}//current density	Capacitance retention	Potential window//electrolyte	Energy density (W h kg^{-1})	Power density (W kg^{-1})	Ref.
1	Co_3O_4/Mn_3O_4	742 F g^{-1} at 1 A g^{-1}	98.6% after 2000 cycles	0 to 0.8 V//1 M KOH	15.3	168.8	67
2	Co_3O_4 porous acicular nanorods	1486 F g^{-1} at 1 A g^{-1}	98.8% after 5000 cycles	0 to 0.45 V//2 M KOH	48.63	600	68
3	Triangular prism shaped Co_3O_4	907.1 F g^{-1} at 1 A g^{-1}	86.5% after 3000 cycles	0 to 0.4 V//6 M KOH	23.0	260	69
4	Co_3O_4 nanowire arrays	746 F g^{-1} at 5 mA cm^{-2}	85% after 500 cycles	−0.05 to 0.38 V//6.0 M dm^{-3} KOH	—	—	70
5	3D Co_3O_4 microstructures	407 F g^{-1} at 1 A g^{-1}	97.5% after 2000 cycles	−0.01 to 0.4 V//6.0 M KOH	—	—	71
6	Co_3O_4 NPs	1273 F g^{-1} at 1 A g^{-1}	96% after 5000 cycles	0 to 0.4 V//5.0 M KOH	—	—	72
7	Co_3O_4 aerogels	>600 F g^{-1} at 1 mg cm^{-2}	96% after 1000 cycles	−0.1 to 0.55 V//1.0 M NaOH	—	—	73
8	Co_3O_4 nanowires	336 F g^{-1} at 1 A g^{-1}	99.1% after 400 cycles	0 to 0.5 V//6.0 M KOH	—	—	74
9	Co_3O_4 nanocrystals	742 F g^{-1} at 0.5 A g^{-1}	86.2% after 2000 cycles	0 to 0.5 V//2.0 M KOH	25.8	125.12	75
10	Co_3O_4 NPs	928 F g^{-1} at 1.2 A g^{-1}	93% after 2200 cycles	−0.2 to 0.4 V//2.0 M KOH	—	—	76
11	Ultralayered Co_3O_4	548 F g^{-1} at 8 A g^{-1}	98.5% after 2000 cycles	−0.2 to 0.5 V//1.0 M KOH	—	—	77
12	Honeycomb like C-Co_3O_4 nanocomposite	94 F g^{-1} at 1 A g^{-1}	88% after 1000 cycles	0 to 0.5 V//1.0 M KOH	—	—	78
13	Flexible nanocellulose/porous Co_3O_4 polyhedron hybrid film	594.8 mF cm^{-2} at 5 mV s^{-1}	64% after 2000 cycles	0 to 0.35 V//6.0 M KOH	18.75	99.97	79
14	Oxygen-deficient Cu-doped Co_3O_4 NPs	180 F g^{-1} at 1 A g^{-1}	92.4% after 5000 cycles	0 to 1.6 V//PVA–KOH	64.1	800	80
15	Mn_3O_4 NPs	401 F g^{-1} at 10 mV s^{-1}	96.9% after 5000 cycles	0 to 1.0 V//1.0 M Na$_2$SO$_4$	40.2	500	81
16	Mn_3O_4/RGO film	52.2 F cm^{-3} at 0.2 A cm^{-3}	115% after 60 000 cycles	0 to 1.8 V//1.0 M Na$_2$SO$_4$	18 mW h cm^{-3}	3.13 W cm^{-3}	82
17	Mn_3O_4 Ni doped film	790 F g^{-1} at 0.5 A g^{-1}	93.6 at 1000	−0.2 to +0.4 V//1.0 M Na$_2$SO$_4$	44.28	162.5	83
18	Mn_3O_4 triangular structures	751.3 F g^{-1} at 1 A g^{-1}	92% after 5000 cycles	0 to 0.8 V//1.0 M Na$_2$SO$_4$	91.7	899.5	84
19	Pyrolytic C/Mn_3O_4 NPs	968 mF cm^{-2} at 0.5 mA cm^{-2}	92% after 5000 cycles	−0.3 to 0.8 V//2.0 M KCl	—	—	85
20	Porous Mn_3O_4 NPs	435 F g^{-1} at 1 mV s^{-1}	90% after 4000 cycles	−0.1 to 0.9 V//1.0 M Na$_2$SO$_4$	—	—	86
21	Mn_3O_4 NPs	823 F g^{-1} at 1 mA cm^{-2}	94% after 10 000 cycles	−1.0 to 1.0 V//1.0 M Na$_2$SO$_4$	88	550	87

in future flexible electronic devices. Two-dimensional (2D) materials exhibit enchanting physiochemical properties important for SC applications. Ultrathin nanosheets provide a high specific surface area due to exposed surface atoms, have more chemically active edge sites rather than basal planes, and better intercalation of electrolyte ions due to open van der Waals gaps. They can be employed in next-generation wearable electronics with higher capacitance, specific capacity, energy density and power density because of their exceptional mechanical strength and flexibility at atomic scales. $NiCo_2O_4$ nanomaterials, for illustration, have recently received much attention as they form a strong interaction with the electrolyte ions and exhibit ultrafast faradaic reactions corresponding to the $Co^{2+}/Co^{3+}/Co^{4+}$ and Ni^{2+}/Ni^{3+} redox combination, and store their charges both on the surface and in the bulk adjacent to the solid electrode's surface. In the next section we will discuss a few of the MTMO spinels for SC applications.

3.2.1. $CuCo_2O_4$ nanostructures. $CuCo_2O_4$ is found in both normal and inverse types of spinel crystal structures. The conversion of normal spinel $CuCo_2O_4$ to inverse spinel $CuCo_2O_4$ takes place when the formula is $Cu_xCo_{3-x}O$ with the x being higher than 0.2.[89,90] $CuCo_2O_4$ has gained attention as it has a high theoretical specific capacitance of 984 F g^{-1} along with high conductivity. $CuCo_2O_4$ shows a higher electrochemical performance than single metal oxides because cobalt cations improve electrochemical activities while copper cations increase electrical conductance. The contribution of Cu in enhancing the electrical conductance is also manifested in other systems, such as in CuCo-LDH by the authors' group recently.[91] There are several reports where different morphologies of $CuCo_2O_4$ were prepared *via* different synthetic routes for SC studies.[92] $CuCo_2O_4$ octahedron NPs were developed using an EDTA-assisted hydrothermal method (Fig. 5a) and also $CuCo_2O_4$ quasi-spheres were developed without the use of EDTA. $CuCo_2O_4$ octahedron NPs exhibited a high specific capacitance of 969 C g^{-1} at 5 mV s^{-1} and an average cycling stability with ~87% retention of the original specific capacitance after 5000 cycles (Fig. 5b and c) compared to $CuCo_2O_4$ quasi-spheres demonstrating their applicability as an active material for SC applications.[93] The capacitance performance was attributed to the exposed (111) crystal facets similar to certain active materials which also have exposed (111) surfaces and showed extraordinary supercapacitor performance. Similarly, an all-solid-state ASC was fabricated using triple-shelled hollow-$CuCo_2O_4$ as the positive electrode, AC as the negative electrode, and polyvinyl alcohol (PVA)/KOH as a gel electrolyte. Interesting TEM images of $CuCo_2O_4$ hollow spheres with different shells were observed at different reaction times (Fig. 5d–f).[94] These hollow spheres were formed by adding the metal precursors to ethylene glycol and isopropanol to form a homogeneous and transparent solution, which was further treated with a hydrothermal procedure at 180 °C and annealing in air at 350 °C. This cell can maintain 80.3 F g^{-1} capacitance at a current density of 2 A g^{-1} and achieved an energy density of 25.2 W h kg^{-1} at a power density of 1.05 kW kg^{-1} (Fig. 6g and h). For faradaic redox reactions,
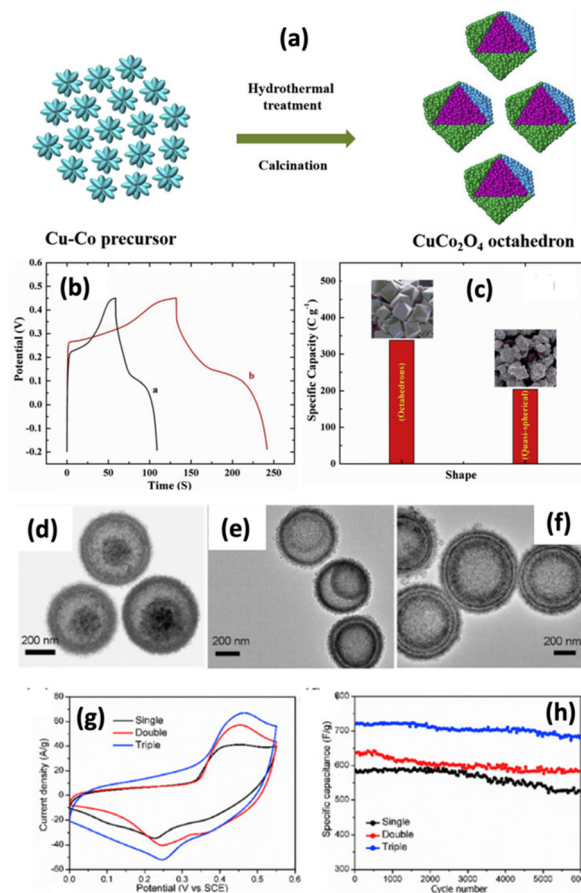

Fig. 5 (a) Schematic procedure for the synthesis of an octahedron-shaped $CuCo_2O_4$ nanomaterial. (b) Comparison of GCD plots of the octahedron and quasi-spherical shaped $CuCo_2O_4$ nanomaterials taken at 2 A g^{-1}. (c) Plot of morphology *vs.* specific capacity (Reproduced from ref. 93 with permission from Elsevier, copyright 2018). TEM images of $CuCo_2O_4$ hollow spheres with different shells obtained with times of (d) 3 h, (e) 6 h, and (f) 8 h, respectively. (g) CV curves of triple-shelled $CuCo_2O_4$ at 50 mV s^{-1} and (h) cycling stability (Reproduced from ref. 94 with permission from Elsevier, copyright 2019).

this unique hollow nanoporous structure provided a sizable surface area with lots of electroactive sites along with synergistic effects between the components for facile electron transfer, short ion diffusion distance, and fast kinetics.[95] Additionally, it was discovered that porous and thin shells were extremely helpful for electrolyte penetration and quick ion/electrode transport, improving the rate performance.[96]

A binder-free $CuCo_2O_4$ nanowire electrode prepared over Ni foam using an electrospinning method depicted a high capacitance (467 mF cm^{-2} at a current density of 1 mA cm^{-1}), with 90% initial capacitance retention after 1500 cycles.[97] Similarly, morphology oriented $CuCo_2O_4$ porous nanostructures (flakes, flowers, blades and wires) were synthesized by varying the solvent and PVP binder concentration as shown in Fig. 6a–d.[98] All the GCD curves are non-linear and symmetric revealing that all the nanostructures show capacitive nature arising from the reversible faradaic redox reactions (Fig. 6e–h). The specific
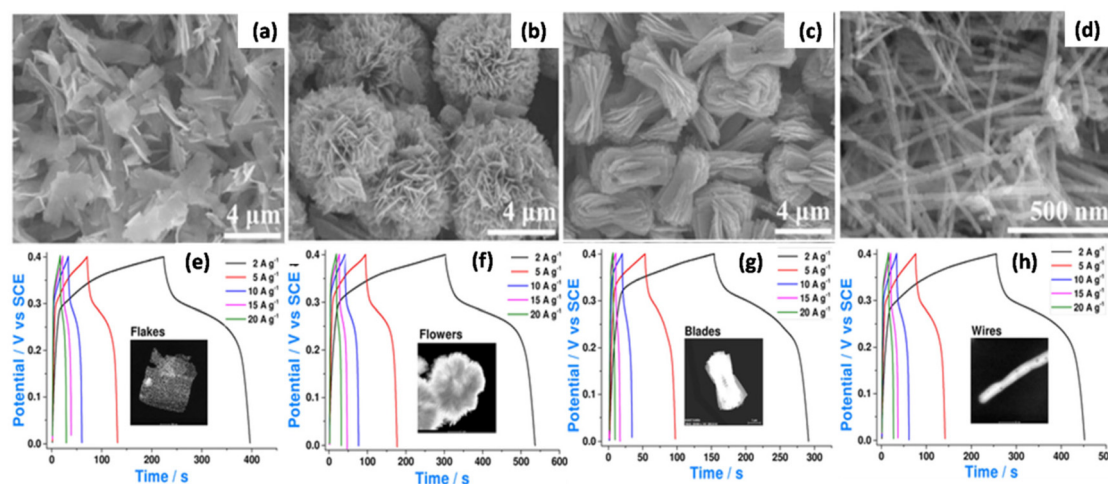
Fig. 6 SEM images of porous CuCo₂O₄ (a) nanoflakes; (b) flowers; (c) blades and (d) wires. (e–h) Corresponding GCD patterns of CuCo₂O₄ with different morphologies (Reproduced from ref. 98 with permission from John Wiley and Sons, copyright 2019).

capacity order was found to be as follows: $CuCo_2O_4$ nanoflowers > $CuCo_2O_4$ nanowires > $CuCo_2O_4$ nanoflakes > and $CuCo_2O_4$ nanoblades, respectively.[98] The high capacitance of $CuCo_2O_4$ nanoflowers over $CuCo_2O_4$-flakes, blades and wires is attributed to the high surface area and porosity after modification in the synthetic route. These uniform 3D $CuCo_2O_4$-nanoflowers facilitate effective faradaic redox reactions due to shorter ion–electron transport lengths and stronger interactions between the electrode and the electrolyte, exhibiting high capacitance and strong cycling stability.

Apart from these reports, $CuCo_2O_4$ is also found to be in different interesting morphologies and offers morphology-oriented charge storage characteristics.[92] Some of these relevant and interesting results are $CuCo_2O_4$ nanobelts showing 487 F g^{-1} within 0–0.45 V with 127% capacity retention,[99] onion-like $CuCo_2O_4$ hollow spheres showing 1700 F g^{-1} within 0–0.4 V with 93.7% capacity retention,[100] double-shelled $CuCo_2O_4$ hollow microspheres showing 1472 F g^{-1} with 93.8% capacity retention,[101] $CuCo_2O_4$ cauliflowers showing 338 F g^{-1} with 96% capacity retention,[102] grass-like $CuCo_2O_4$/NFs showing 611 F g^{-1} with 98% capacity retention,[103] and chestnut-like $CuCo_2O_4$/NFs with 1256 F g^{-1}, within the 0–0.4 V potential window and 85.2% capacity retention after a few thousands of cycles.[104]

All these examples of morphology-oriented nanostructured $CuCo_2O_4$ manifested that morphology plays a crucial role in EES cells. This is the same for other TMOs too. However, it is difficult to classify all the properties according to a specific morphology. Notwithstanding, it can be stated that NPs with 2D morphology having maximum exposed active surfaces, high surface areas, porous structures, and high energy facets are essential and common factors in all cases. These properties help in the intercalation of electrolyte ions in a better way and provide more space for redox reactions.

3.2.2. ZnCo₂O₄ nanostructures. Similar to other first row transition metals, Zn is also used for developing binary metal

oxide spinels and further examined for energy storage applications. $ZnCo_2O_4$ is considered as a good candidate for supercapacitor applications owing to its uniform porous nature, better reversible capacities, good cycling stability and non-toxic nature. $ZnCo_2O_4$ microspheres having a surface area of 36 m^2 g^{-1} and an average pore size of 6.96 nm deliver a specific capacitance of 542.5 F g^{-1} at a current density of 1 A g^{-1} and good stability up to 2000 cycles.[105] A $ZnCo_2O_4$-rGO composite with a mesoporous sheet-like morphology *via* a nickel substrate was developed using a hydrothermal method (Fig. 7a and b).[106] A suitable faradaic reaction of the $ZnCo_2O_4$ component was ensured by the hierarchically porous texture of the $ZnCo_2O_4$-rGO composite with a high surface area and effective ion diffusion channels. Therefore, the $ZnCo_2O_4$-rGO// AC ASC offered relatively high specific capacitance (Fig. 7c) and the asymmetric cell delivered a high energy and power density of 49.1 W h kg^{-1} and 400 W kg^{-1}, respectively, and attained 93% capacitance retention after 5000 cycles as shown in Fig. 7(d).[106] Here, it was suspected that the mesoporous microspheres can largely increase the number of electroactive sites and provide extra free space to effectively alleviate the structural strain that positively interferes with the charge–discharge process, and hence high reversible capacity and cyclability.[105,107] A deep eutectic solvent (DES)-mediated ionothermal process was applied for the synthesis of porous $ZnCo_2O_4$ nanoflakes. The $ZnCo_2O_4$//AC ASC exhibits highly interesting stability, with no capacitance loss up to 10 000 cycles (Fig. 7e).[108]

The facile synthesis of $ZnCo_2O_4$ nanowire cluster arrays (NWCAs) on Ni-foam was also performed for this high-performance ASC. The NWCAs on Ni foam were directly used as integrated electrodes for supercapacitors and exhibited a high specific capacitance of 1620 F g^{-1} at 8 A g^{-1} in 3 M KOH aqueous solution, and an excellent cycling stability at various current densities up to 100 mA cm^{-2} (at 40 A g^{-1}), with 90% of the initial capacitance being retained after 6000 cycles.[109] In a
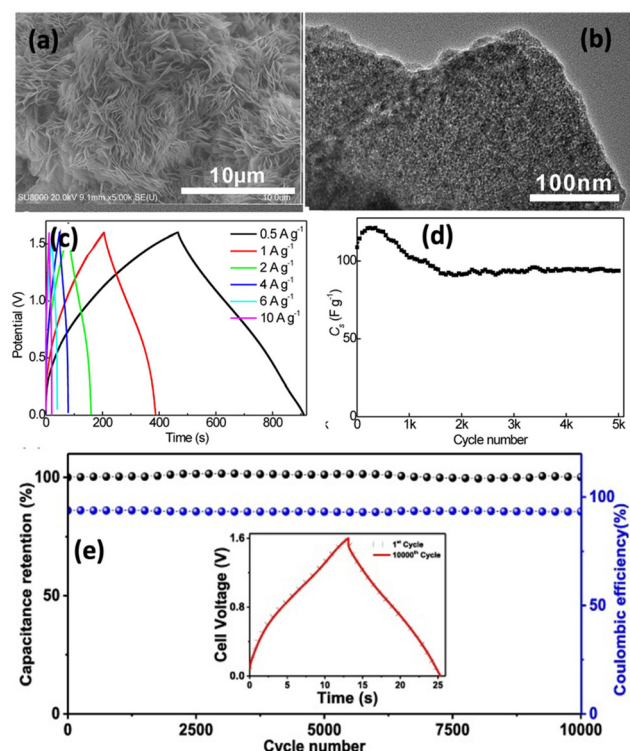
Fig. 7 (a and b) SEM and TEM images of $ZnCO_2O_4$ attained sheet-like morphology. (c) GCD curves at different current densities from 0.5 to 10 A g^{-1}. (d) Retention of specific capacitance up to 5000 cycles (Reproduced from ref. 106 with permission from Elsevier, copyright 2018). (e) Cycling stability of the $ZnCo_2O_4$//AC ASC. Capacitance retention and coulombic efficiency with respect to the cycle number. The inset shows the GCD curves of the 1st and 10 000th cycles (Reproduced from ref. 108 with permission from Elsevier, copyright 2021).

binder free ASC made-up of $ZnCo_2O_4$ nanoflowers on a 3D CNT/nitrogen-doped graphene film ($ZnCo_2O_4$/NGN/CNT) demonstrated a superior specific capacitance (1802 F g^{-1}), energy density ($\approx$37.19 W h kg^{-1} at 750 W kg^{-1}) and power density ($\approx$14.992 kW kg^{-1} at 14.16 W h kg^{-1}).[110] The electrochemical results of these zinc cobaltite and carbon based hybrids are attributed to (a) a large number of active sites for the faradaic reaction and readily accessible electrolyte ion passageways for quick transportation; (b) an improved rate of electrolyte ion contact with the NGN/CNT film; and (c) the presence of pyridine nitrogen, which could increase the wettability between the electrode materials and electrolyte ions and improve graphene's electrical conductivity, leading to an increase in specific capacitance.[109,110] Similarly, the hierarchical $ZnCo_2O_4$/nickel foam structure retained the original nickel foam's outstanding elasticity, making it easier to create wearable technology for flexible energy storage applications. It exhibited outstanding electrochemical performance in supercapacitors with high specific capacitance ($\sim$1400 F g^{-1} at 1 A g^{-1}), rate capability (72.5% capacity retention at 20 A g^{-1}), and good cycling stability at 6 A g^{-1}.[111] The source of total capacitance arises primarily from the redox pseudo-capacitance of the loaded porous $ZnCo_2O_4$ nanorods and 1D shape. The 1D

$ZnCo_2O_4$ active material gets stuck tightly to the nickel foam achieving excellent adhesion and electrical contact. They also confirmed that the as-prepared structures can be employed in high power density applications, such as electric vehicles, flexible electronics, and energy storage devices, in addition to high energy density domains.

Thereafter, $ZnCo_2O_4$ with various nanostructured morphologies have been exploited for SC applications. Some of these interesting applications are: mesoporous, hierarchical core/shell structured $ZnCo_2O_4$/MnO_2 nanocone forests for high-performance SCs;[112] urchin-like $ZnCo_2O_4$ microspheres assembled from nanowires on Ni-foam for SCs;[113] porous $ZnCo_2O_4$ films by successive ionic layer adsorption for solid-state symmetric SC devices;[114] porous thin layered nanosheet assembled $ZnCo_2O_4$ grown on Ni-foam for hybrid SCs;[115] $ZnCo_2O_4$ micro-flowers and micro-sheets on Ni-foam for pseudocapacitor electrodes;[116] free-standing 2D mesoporous $ZnCo_2O_4$ thin sheets consisting of 3D ultrathin nanoflake array frameworks for ASCs;[117] a $ZnCo_2O_4$–reduced graphene oxide composite with balanced capacitive performance in ASCs;[118] *etc*. All these reports reminded that the mixed metal oxidation states of cobalt in $ZnCo_2O_4$ play a crucial role in enhancing the EES properties.

3.2.3. $NiCo_2O_4$ nanostructures. With some of the great features, such as high theoretical capacity (greater than 3000 F g^{-1} or 891 mA h g^{-1}), relatively low cost and natural abundance, and ease of synthesis, nickel-cobalt oxide ($NiCo_2O_4$) has emerged as a new type of energy storage material for electrochemical SCs. $NiCo_2O_4$ also known as 'nickel cobaltite' is a mixed transition metal oxide belonging to the class of the spinel family with an inverted spinel structure.[119] Similar to other MTMOs, $NiCo_2O_4$ NPs too can be synthesized by various preparation techniques such as hydrothermal, solvothermal, high temperature colloidal, sol–gel, and also solid state synthesis methods.[120] At the beginning, Hu *et al.* prepared $NiCo_2O_4$ *via* a sol–gel process by forming nickel cobaltite aerogels with the epoxide-addition procedure, followed by drying in supercritical carbon dioxide.[121] The propylene oxide/metal-ion molar ratio was 11 : 1 and the dried aerogel was further calcined at 200–300 °C for 5 h to convert the metal hydroxides to oxides. The obtained mesoporous NPs were targeted for EES, which manifests an ultrahigh specific capacitance of 1400 F g^{-1} due to the high specific surface area, porosity, electronic conductivity, electrochemical activity and multiple oxidation states/structures.[121] Thereafter, there were several advancements where $NiCo_2O_4$ was used as a promising EES electrode material. The exceptional behavior of this $NiCo_2O_4$ material can be attributed to the redox reaction that occurs at the electrode surface during the charge storage mechanism in an aqueous medium as shown below.

$$NiCo_2O_4 + OH^- + H_2O \leftrightarrow 2NiOOH + 2CoOOH + e^- \quad (3)$$

$$CoOOH + e^- \leftrightarrow CoO_2 + H_2O + e^- \quad (4)$$
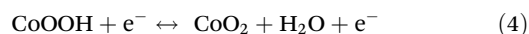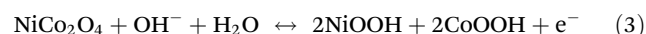
Nanostructured $NiCo_2O_4$ with various morphologies were prepared over the decade, which showed diverse and interest-

ing SC performances mainly attributed to reduced interfacial polarization, high ion diffusion, composite formation, and reduced charge transfer resistance.[122,123] Yet and unfortunately, in most cases the observed charge storage characteristics have faced issues such as (i) low specific capacitance, (ii) narrow potential window, (iii) low cycling life, and (iv) low power and energy density. To overcome all these issues, novel approaches have been adopted to develop new $NiCo_2O_4$ NPs as an excellent electrode material with new optimized synthetic methods which positively address all these issues.

In some key developments, Deka and co-workers developed two-dimensional and three-dimensional $NiCo_2O_4$ nanostructures (hexagonal platelets, coral-shaped and octahedron NPs) which demonstrated excellent battery type energy storage activity due to the ultra-fast intercalation reaction of electrolyte ions with nickel cobaltite at the electrode surface.[124–126] In terms of a traditional three-electrode approach and a coin-cell device, the material's charge storage capabilities and dependability as an active electrode have been established. The $NiCo_2O_4$ hexagonal nanoplatelets have an average diameter of 65 nm as shown in Fig. 8a with a high specific surface area of 59 m^2 g^{-1} and a pore volume of 0.44 cm^3 g^{-1}. This $NiCo_2O_4$ offered 1084 to 300 F g^{-1} C_{SP} at different current densities and were 98% stable up to 20 000 measured GCD cycles (Fig. 8d). These high performances were attributed to the ultrafast intercalation reaction of electrolyte ions with nickel cobaltite at the electrode surface.[124,126] 50–60 nm monodisperse perfect octahedron NPs without any structural deformation were prepared using a low-cost hydrothermal method (Fig. 8b). This material delivered a battery like faradaic capacitance of 516 F g^{-1} at a current density of 13.68 A g^{-1} (Fig. 8e) and a high energy density (16.33 W h kg^{-1}) and power density (2800 W kg^{-1}).[125] Faster ion switching across the electrode–electrolyte interface, NP based extrinsic-pseudocapacitance and preferably the octahedron morphology (high packing) of the electrode material are attributed to the driving force for the observed outstanding SC performances.

Interesting coral-shaped $NiCo_2O_4$ NPs were prepared using the oriented attachment pathway of nanocrystal building blocks where the less stable and highly reactive (111) planes of $NiCo_2O_4$ small single crystals were grown at the expense of the (100) planes in the <111> direction to reduce the total interfacial free energy and become attached to each other leading to the formation of coral-shaped nanostructures (Fig. 8c).[126] Their exceptional supercapacitive behavior (maximum C_{SP} 1297 F g^{-1}, energy density 45 W h kg^{-1} and minimum stability of 10 000 cycles) was ascribed (Fig. 8f) to the faster switching of ions between the electrode material and the electrolyte, the high surface area, and the high porosity reducing the diffusion distances.[126] Therefore, $NiCo_2O_4$ two- and three-dimensional nanostructures facilitate faster charge-transfer routes ensuring lower contact resistance and thus act as a potent material for advanced energy storage applications.

Developing and synthesising $NiCo_2O_4$ with interesting and novel morphologies for excellent SCs still remain a hard task. $Co_3O_4/NiCo_2O_4$ double-shelled nanocages (DSNCs) or box-in-box nanocages from ZIF-67 were prepared and this novel morphology not only showed efficient SC performances, but the cell was also stable up to 12 000 cycles (Fig. 9a and b).[127] Gao and co-workers described a modified hydrothermal method to synthesize hierarchical porous $NiCo_2O_4$ microboxes (Fig. 9c). In electrochemical supercapacitor applications, hollow mor-
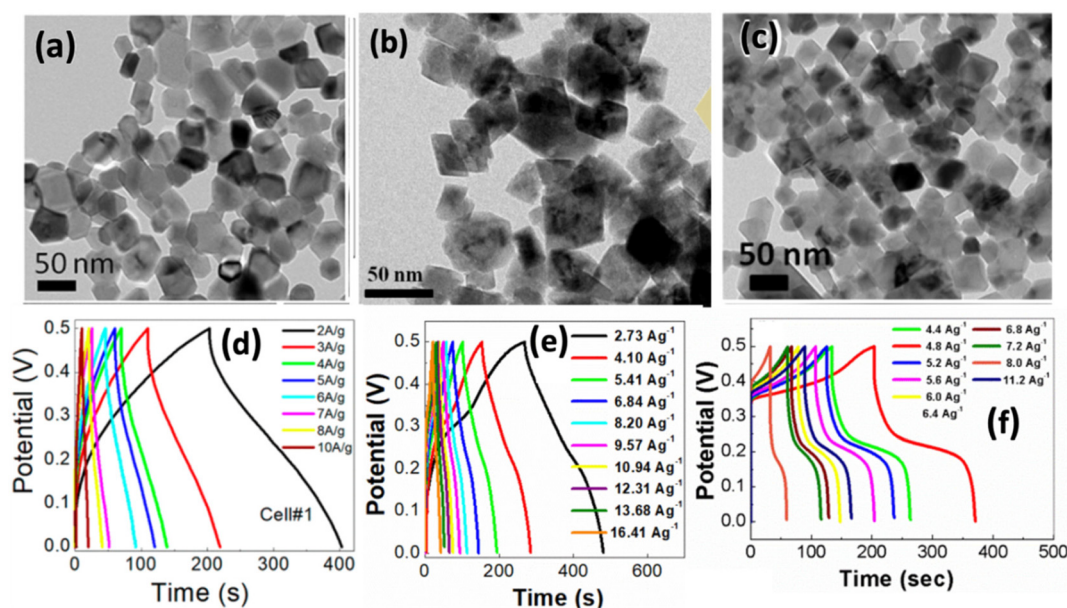

Fig. 8 TEM image of $NiCo_2O_4$ nanostructures: (a) hexagonal nanoplatelets, (b) octahedra and (c) coral-shaped synthesized by various synthetic routes. Corresponding GCD patterns of $NiCo_2O_4$ nanostructures: (d) hexagonal nanoplatelets, (e) octahedra and (f) coral-shaped (Reproduced from ref. 124, 125 and 126 with permission from American Chemical Society, copyright 2018, 2019, 2020).
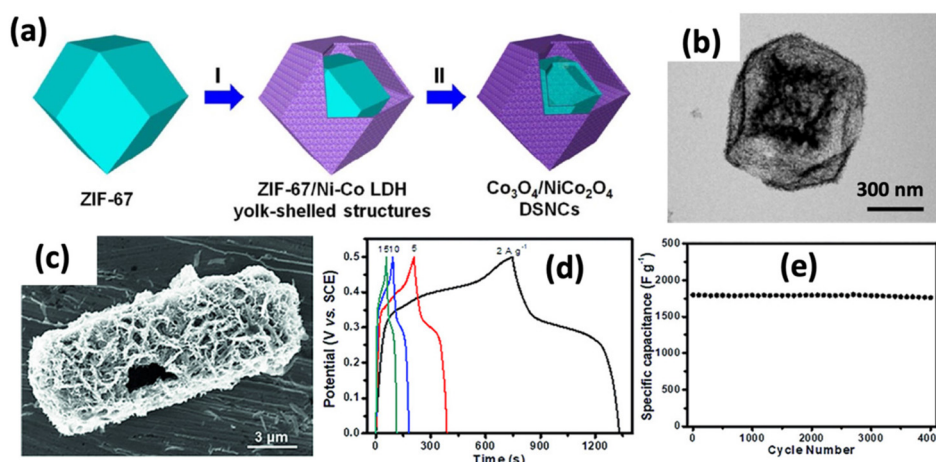
Fig. 9 (a) Schematic illustration of the formation process of $Co_3O_4/NiCo_2O_4$ DSNCs and (b) TEM image of an individual $Co_3O_4/NiCo_2O_4$ DSNC (Reproduced from ref. 127 with permission from American Chemical Society, copyright 2015). (c) FESEM images of $NiCo_2O_4$ boxes having a size in micrometres. (d) GCD curves at different current densities (2, 5, 10 and 15 A g^{-1}). (e) Cycling stability test up to 4000 cycles (Reproduced from ref. 128 with permission from John Wiley and Sons, copyright 2020).

phology, rich active sites, high ion transportation and the surface area play significant roles in achieving high capacitance. These $NiCo_2O_4$ systems delivered a capacitance of 1820 F g^{-1} and 96.6% capacitance retention after 4000 cycles at a current density of 5 A g^{-1} (Fig. 9d and e), concluding that hollow or porous structures are highly desirable to achieve high capacitance values. The literature of $NiCo_2O_4$ on a three-electrode and two-electrode coin cell study is very rich, hence, here we will discuss a few more highly interesting reports which gained attention from the community due to their new features. Some of them are: interaction based $NiCo_2O_4$@polyaniline nanotube heterostructures anchored on carbon textiles,[129] "OH– ion-buffering-reservoir" based electromechanical stability in $Co_3O_4/NiCo_2O_4$ perforated nanosheets,[130] synergistic effect and stable structure based highly stable Ni–Mn–oxide,[131] ZIF-derived $Ni_xCo_{3-x}O_4$ nanotube array hierarchical structures based on the self-assembly of 1D and 2D structures (crosslinking structures provide large surface areas and more active sites),[132] morphology controlled urchin-like porous hierarchical $NiCo_2O_4$/RGO electrodes,[133] KCu_7S_4@$NiCo_2O_4$ *in situ* grown on Ni-foam and asymmetric KCu_7S_4@$NiCo_2O_4$//AC (high energy density of 125.56 W h kg^{-1})[134] flower-like $NiCo_2O_4$@$Ni(OH)_2$/NiOOH composites supported on Ni-foam by the green solvent dimethyl sulfoxide,[135] *etc.* including other bifunctional, hierarchical and exotic Ni–Co–O NPs.[136,137] All these results argued that $NiCo_2O_4$ has the upper hand over the other TMOs at least in SC applications. A few of the MTMOs' electrochemical performances are compared in Table 2.

4. Commonly used electrolytes with spinel oxides

For SC applications, electrolytes play a crucial role as they provide an ionic medium for charge movement processes.[159]

An ideal electrolyte for SC applications is the one that has high ionic conductivity, a wide potential window, electrochemical stability and inertness, thermal stability, low volatility and non-flammability properties. Such an ideal electrolyte is also eco-friendly, non-expensive and compatible with electrode materials. The SC applications involve several electrolytes, such as aqueous, organic, ionic liquids (IL), and solid polymers,[160] which are used to fabricate different types of devices in combination with MTMO spinels. In the next sections we will discuss these popular electrolytes according to the classifications.

4.1. Aqueous electrolytes

Aqueous electrolytes can be prepared and employed without too tight control of the production process. As the name suggests, water acts as the popular solvent in this case. Aqueous electrolytes provide higher ionic concentrations, possess higher conductivity (*e.g.*, 0.8 S cm^{-1}) and lower resistance compared to other electrolytes due to its low dynamic viscosity.[160,161] However, the potential window range of aqueous electrolytes is narrow (~1.23 V) due to the thermodynamic decomposition of water, yet they are employed for energy-storage applications due to their unprecedented advantages.[162] The aqueous electrolytes can be categorized into three types: (i) acidic solution, where H_2SO_4 is the most prominent one as it not only has high ionic conductivity/concentration but also low equivalent series resistance. Therefore, adding redox additives to H_2SO_4 aqueous solution is a good way to optimize the electrolyte and improve the performance of MTMO spinel SCs. (ii) Alkaline solution, *e.g.* KOH, NaOH, and LiOH. Out of these KOH is found to be most frequently used and the best choice in MTMO based SCs. (iii) Neutral solution, where the most frequently used aqueous electrolytes with MTMO are Na_2SO_4, KCl, Li_2SO4, $(NH_4)_2SO_4$, K_2SO_4, Li_2SO_4, $MgSO_4$, NaCl, KNO_3, *etc.*[163]

Table 2 Comparison of the electrochemical performance of mixed TMOs spinel materials

Sl. no.	Electrode material	C_{SP} at current density	Capacitance retention	Potential window//electrolyte	Energy density (W h kg^{-1})	Power density (W kg^{-1})	Ref.
1	Bundle-like CuCo$_2$O$_4$ microstructures	303.22 C g^{-1} at 1 A g^{-1}	69.77% after 5000 cycles	0 to 0.4 V//2.0 M KOH	39.95	944.63	138
3	CuCo$_2$O$_4$ NPs	401.2 C g^{-1} at 0.5 A g^{-1}	82.5% after 10 000 cycles	0 to 0.5 V//2.0 M KOH	29.5	832.6	139
4	Porous CuCo$_2$O$_4$ microtubes	393.6 C g^{-1} at 1 A g^{-1}	82.5% after 3000 cycles	0 to 0.55 V//2.0 M KOH	—	—	140
5	CuCo$_2$O$_4$ nanosheets	134.5 C g^{-1} at 1 A g^{-1}	104.2% after 3000 cycles	0 to 1.75 V//2.0 M KOH	36.16	1010	141
6	Mesoporous CuCo$_2$O$_4$ nanowires	1210 F g^{-1} at 2 A g^{-1}	64% after 4000 cycles	0 to 0.5 V//6.0 M KOH	42.8	15 000	142
7	Porous ZnCo$_2$O$_4$ NPs	776.2 F g^{-1} at 1 A g^{-1}	84.3% after 1500 cycles	0 to 0.45 V//2.0 M KOH	84.4	400	143
8	ZnCo$_2$O$_4$ NPs	462.5 C g^{-1} at 1 A g^{-1}	97.4% after 5000 cycles	0 to 0.4 V//2.0 M KOH	—	—	144
9	Hollow ZnCo$_2$O$_4$ microspheres	78.89 mA h g^{-1} at 1 A g^{-1}	56% after 2000 cycles	0 to 0.5 V//3.0 M KOH	—	—	145
10	ZnCo$_2$O$_4$/C core–shell nanowire arrays	2340 F g^{-1} at 20 mA cm^{-2}	92.6% after 10 000 cycles	0 to 0.5 V//2.0 M KOH	35.75	7317	146
11	CuCo$_2$O$_4$ nanorods	713 F g^{-1} at 11 mA cm^{-2}	~90% after 5000 cycles	—	37.43	250	147
12	Hexagonal NiCo$_2$O$_4$ NPs	1525 F g^{-1} at 1 A g^{-1}	98% up to 2000 cycles	0 to 0.4 V//2.0 M KOH	24.5	175	148
13	NiCo$_2$O$_4$ embedded carbon nanofibers	836 F g^{-1} at 5 A g^{-1}	80.9% up to 2000 cycles	0 to 0.5 V//6.0 M KOH	—	—	149
14	Self-assembled NiCo$_2$O$_4$ NPs	225.07 C g^{-1} at 0.5 A g^{-1}	86.9% up to 2000 cycles	0 to 0.35 V//1.0 M KOH	19.12	509.87	150
15	NiCo$_2$O$_4$ nanoarrays	12.3 F cm^{-2}	83.1% up to 2000 cycles	0 to 0.6 V//1.0 M KOH	—	—	151
16	NiCo$_2$O$_4$ nanorods	440 F g^{-1} at 5 A g^{-1}	94% up to 2000 cycles	0 to 0.5 V//2.0 M KOH	12.6	4003	152
17	C@NiCo$_2$O$_4$ hollow microspheres	404 F g^{-1} at 1 A g^{-1}	87.1% up to 1000 cycles	0 to 0.5 V//6.0 M KOH	—	—	153
18	NiCo$_2$O$_4$ nanorods	697.5 F g^{-1} at 1 A g^{-1}	85.77% up to 10 000 cycles	0.14 V–0.55 V//2.0 M KOH	—	—	154
19	Ultrathin NiCo$_2$O$_4$ nanosheets	922.9 C g^{-1} at 1.0 A g^{-1}	95.5% up to 5000 cycles	0 to 1.6 V//6.0 M KOH	39.1	799.9	155
20	Honeycomb-like NiCo$_2$O$_4$@Ni foam	646.6 F g^{-1} at 1.0 A g^{-1}	96.5% up to 3000 cycles	0 to 0.5 V//2.0 M KOH	48	1076	156
21	Hierarchical NiCo$_2$O$_4$@NiO composites	1188 F g^{-1} at 2 A g^{-1}	106.8% up to 7000 cycles	0 to 0.5 V//1.0 M KOH	—	—	157
22	P-doped NiCo$_2$O$_4$ nanowires	2747.8 F g^{-1} at 1 A g^{-1}	50% up to 5000 cycles	0 to 0.5 V//6.0 M KOH	28.2	7750.3	158

4.2. Non-aqueous electrolytes

Organic electrolytes and ionic liquid (IL) electrolytes are non-aqueous type electrolytes used with MTMO spinels in SCs to increase the voltage window (up to 3.0 V) and stability. Organic electrolytes typically consist of conducting salts dissolved in organic solvents (acetonitrile, CAN and propylene carbonate, PC). Tetraethylammonium tetrafluoroborate (TEABF$_4$) in PC and ACN are some commonly used organic electrolytes.[164] Similarly, ILs have also gained significant attention, and are defined as molten salts at room temperatures having characteristic features of low vapour pressure, high thermal stability, excellent ionic conductivity, wide potential window (0.0–3.0 V), non-flammability and eco-friendliness. Thus, IL electrolytes circumvent the disadvantages related to the most common electrolytes, hence there is an indispensable need to incorporate ionic liquids (ILs) into the MTMO spinel electrodes and replace the aqueous and organic electrolytes to achieve excellent performance of the EES devices. Some of the popular ILs for SCs are 1-ethyl-3-methylimidazolium trifluoromethanesulfonate [EMIM] [TRIFLATE], 1-ethyl-3-methylimidazolium tetrafluoroborate [EMIM][BF$_4$] and 1-hexyl-3-methylimidazolium hexafluorophosphate [HMIMPF$_6$].[24,165,166] Nonetheless, despite several advantages, the major drawback of IL electrolytes is their high cost which limits their application at the commercial scale.

4.3. Solid state and redox active electrolytes

Solid-state electrolytes have advantages over other electrolytes such as good ionic conducting media, simple packaging, and liquid-leakage free components. In addition, for the fabrication of blended and flexible SCs with MTMOs, solid-state electrolytes appear to be the best choice.[167] Moreover, the capacitance of supercapacitors can be increased by inducing pseudocapacitive contribution in the case of redox-active electrolytes. However, these types of electrolytes are rarely explored with MTMOs for SC applications.[168,169]

5. MTMO based flexible supercapacitors

Flexible, lightweight, bendable and wearable patch devices or SC devices composed of a TMO based electrode material have attracted immense attention for their potential commercial application. Fabrication of a flexible SC cell has many limitations, starting from the stiffness of substrates and current collectors, leakage of electrolytes, lower areal capacitance, strain and stress related to the mechanical stability of the entire cell, *etc*. To overcome all these limitations, a lot of research has been done and are discussed further in this review covering a few of the majorly explored MTMO based flexible devices. Out of these examples, NiCo$_2$O$_4$ is found to be extensively studied, because it is low-cost, has high thermal and chemical stability, good electrical conductivity, feasible oxidation states/structures, high specific area and pore volume, low charge-transfer

resistance and low interaction time with the electrode/electrolyte interface.[170] Due to these features, $NiCo_2O_4$ has been found superior to other TMOs. Similar to the three-electrode cell and the coin cell, flexible supercapacitors too can use a non-faradaic energy storage process (EDLC) or a faradaic mechanism (surface or diffusion controlled).

There have been several works on $NiCo_2O_4$ based flexible devices as they are cost-effective, environment-friendly, and show high electrochemical performance due to their MTMO nature.[171] Flexible cells, where $NiCo_2O_4$ NPs are grown on different substrates such as carbon fiber paper, Ni-foam, and Ti-sheets showed good cycling stability, power density and high capacitance.[171–173] Highly flexible symmetric and asymmetric solid-state supercapacitor devices were fabricated by sandwiching electrodes of morphology oriented $NiCo_2O_4$ nanocrystals on various substrates.[174–176] These devices showed excellent EES performances including cycling stability and rate capability, suggesting that the $NiCo_2O_4$ electrode material is highly suitable for the fabrication of high-performance flexible supercapacitor devices working at variable temperatures.

A flexible carbon/$NiCo_2O_4$ network was prepared by an electrospinning method along with *in situ* carbonization to gain flexibility using a PAN/PVP binder.[177] Fig. 10a shows the SEM image of the carbon/$NiCo_2O_4$ network. The growth of the porous $NiCo_2O_4$ nanotube by electrodeposition on carbon nanofibers was done in order to fabricate flexible electronic and wearable flexible devices. The fabricated flexible electrode delivers a maximum specific capacitance of 1403.5 F g^{-1} at 1.0 A g^{-1} current density and 95.7% cycling stability up to 2000 cycles. Fig. 10b depicts the folding capability and cycling stability of the as-prepared flexible cell from this work. The present author's group also developed all solid-state flexible SC devices having high mechanical strength and bending stability features with the help of a solid electrolyte cum separator and $NiCo_2O_4$ octahedral NPs (the TEM image is shown in Fig. 8b).[125] For making an effective flexible cell assembly, a flexible substrate was first prepared. A flexible separator cum electrolyte was prepared using [EMIM][BF_4] and PVDF precursors and the schematic cross-section of the cell is shown in Fig. 10c. The device exhibited a high specific capacity (97.9 mA h g^{-1}) and capacitance value (117.3 F g^{-1}) at a current density of 0.625 A g^{-1}operated at a high potential window (3.0 V) as shown in Fig. 10d. No kind of deformation was observed and the LEDs were also lit at different bending angles (Fig. 10e).[125] It is found that a successful integration of MTMOs with ionic liquid electrolytes provides several advantages such as high thermal stability, chemical and electrochemical stability, negligible volatility, and nonflammability, which could not be found with other electrolytes for flexible SCs. Flexible carbon cloth is also found to be an interesting substrate in SC devices. An assembled all-solid-state symmetric supercapacitor cell of $NiCo_2O_4$ NPs with a PVA–H_2SO_4 gel electrolyte offered a high energy density of 2.07 mW h cm^{-3} at a current density of 2 mA cm^{-2}.[179] The CV curves of this cell at different bending states and the pictorial representation of the flexible device developed using a nickel wire are shown in Fig. 10f.[178] A sandwich-
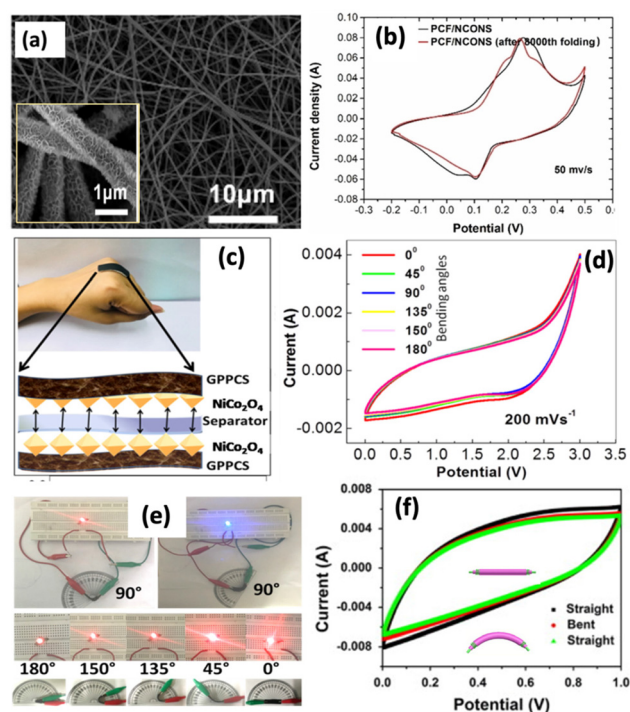

Fig. 10 (a) SEM image of $NiCo_2O_4$ nanosheets grown over carbon nanofiber. (b) CV curves of before and after 8000th folding of the flexible cell at a scan rate of 50 mV s^{-1} (Reproduced from ref. 177 with permission from John Wiley and Sons, copyright 2021). (c) Demonstration of a flexible solid-state wearable supercapacitor patch device. (d) CV curves of the flexible device at different bending angles at a scan rate of 200 mV s^{-1}. (e) Lighting of different colour LED lights using the cell connected in series (Reproduced from ref. 125 with permission from American Chemical Society, copyright 2019). (f) CV curves in different bending states and pictorial representation of the flexible device of $NiFe_2O_4$ fabricated on a nickel wire (Reproduced from ref. 178 with permission from Elsevier, copyright 2014).

like CNTs/$NiCo_2O_4$ hybrid paper flexible electrode consisting of a layer of conductive CNT buckypaper coated with honeycomb-like $NiCo_2O_4$ nanosheets at both sides was developed which exhibited almost identical CV curves at different bending angles.[176] At 0.1 mA cm^{-1} current density, the calculated areal capacitance was found to be 337.3 mF cm^{-1} and the specific capacitance was found to be 268.4 F g^{-1}. The flexible device shows a very slow decrease of specific capacitance after 2000 GCD cycles at a current density of 2 mA cm^{-1}. One or more key factors, such as, (a) a faster ion intercalation between the electrode and the electrolyte interface, (b) ultrafast faradaic reactions corresponding to the Co^{2+}/Co^{3+} and Ni^{2+}/Ni^{3+} redox couples, (c) surface area and porosity related to the morphology and (d) ability to store charges both on the surface and in the bulk near the surface of the solid electrode, are found to be responsible for the high-performance charge storage of these $NiCo_2O_4$ based flexible SCs.

Apart from $NiCo_2O_4$, other MTMOs were also used to fabricate flexible SC devices. $NiFe_2O_4$ NPs were directly grown on a flexible carbon cloth (CC) substrate by a facile surfactant-

assisted hydrothermal method.[180] Here, to address the issue of serious aggregation, the low specific surface area of active sites and the low specific capacitances of $NiFe_2O_4$, the active material was directly grown on three-dimensional conductive CC substrates. The assembled all-solid-state symmetric supercapacitor cell showed a voltage window of 2 V using PVA–H_2SO_4 as the gel electrolyte and offered a high current density of 2.07 mW h cm^{-3} at 2 mA cm^{-2} current density. A flexible symmetric supercapacitor device was manufactured using two $NiFe_2O_4$ nanosheet electrodes (SS/$NiFe_2O_4$ nanosheets (+)//$NiFe_2O_4$ nanosheets (−)/SS) using the PVA–KOH solid-state electrolyte.[181] Faradaic redox charge storage behavior and symmetrical CV curves without apparent polarization were observed, indicating the fast charging–discharging and excellent reversibility of flexible SCs. Vadiyar et al. fabricated a flexible solid state asymmetric device by the reflux condensation mediated deposition of Co_3O_4 nanosheets and $ZnFe_2O_4$ nanoflakes.[57] This device delivers a maximum specific capacitance of 156 F g^{-1}, a maximum energy density of 36 W h kg^{-1} at a higher power density of 8.8 kW kg^{-1} along with 98% retention of the original capacitance over 12 000 cycles. The same group has also prepared another flexible asymmetric cell with low cost 3-D aligned and cross-linked $ZnFe_2O_4$ nano-flakes as the negative electrode and $Ni(OH)_2$ as the positive electrode. The cell sustained capacitance at varying degrees of bending angles with smaller relaxation times and response frequencies.[182]

$CuCo_2O_4$ also remains an attractive material for flexible device applications. $CuCo_2O_4$ nanowires were used to prepare a highly flexible ASC device using polypyrrole (PPy) as the counter electrode on a CNT yarn substrate.[183] The flexible ASC of $CuCo_2O_4$@CQD//Fe_2O_3@CQD (carbon quantum dot, CQD) configuration on graphite paper delivers a high operation voltage of 1.55 V, a high capacitance of 288.3 C g^{-1} at 1 A g^{-1}, an energy density of 39.5 W h kg^{-1} at 1203.7 W kg^{-1}, and a long cycling life and high rate capability.[184] $CuCo_2O_4$ was used with other metal oxides too to form high performance ASC cells. For instance, an ASC cell derived from core–shell $CuCo_2O_4$@MnO_2 nanowires on carbon fabrics delivered 714 mF cm^{-2} capacitance at 1 mA cm^{-2} current density. It also delivered a high energy density of 94.3 W h cm^{-2} at a power density of 0.4757 mW cm^{-2} for a voltage window of 1 V.[185] MnO_2 nanoflakes are vertically grown on $CuCo_2O_4$ nanosheets to form a core–shell architecture on Ni foam. The $CuCo_2O_4$@MnO_2 arrays and activated graphene (AG) were tailored to the same size and then assembled together with a separator and electrochemical measurements were performed in 1.0 M Na_2SO_4 electrolyte. This flexible device worked in a wide voltage region as high as 2.0 V and exhibited a specific capacitance of 78 F g^{-1} at a current density of 1 A g^{-1} with a maximum energy density of 43.3 W h kg^{-1}.[186] Some other flexible SC devices based on $CuCo_2O_4$ are $CuCo_2O_4$@$Ni(OH)_2$ 3D hierarchical core–shell structure,[187] peculiar 3D interconnected aligned porous nanowall morphology of $CuCo_2O_4$,[188] etc. $ZnCo_2O_4$ nanorods on a Ni wire as the fiber electrode were prepared using a simple and rapid single-step hydrothermal process. This flexible supercapacitor exhibited remarkable electrochemical stability when subjected to bending at various angles.[189] Another all-solid-state, lightweight, and flexible ASC was prepared using cabbage-like $ZnCo_2O_4$ as the positive electrode material, porous VN nanowires as the negative electrode material, and flexible CNT films as the collector. This device offered a specific capacitance of 196.43 mF cm^{-2}, a large voltage window of 1.6 V, and a volume energy density of 64.76 mW h cm^{-3} with 100% coulombic efficiency and mechanical stability.[190] All these mentioned high performances are attributed to the superior electrochemical stability of the MTMOs, a quicker infiltration process of the electrolyte by decreasing the transmission time of ion penetration, faster switching of electrolyte ions, high rate of adsorption/desorption of ions, high surface area, and low charge transfer resistance. Hence, flexible supercapacitors remain highly attractive for a large number of emerging portable lightweight consumer devices, and mixed transition metal oxide based working electrodes play a crucial role in these devices.

6. Outlook and challenges

In this review article, we focused mainly on the mixed transition metal oxides for supercapacitor applications, which offer high capacitance with longer cycling lives, higher energy and power densities, and faster charge–discharge capabilities due to their internal quick ion switching properties. These properties make them one of the most promising EES materials. It is found that the nanostructured MTMOs positively address issues like non-matching uncertainties between electrode materials and innovative electrolytes, low energy density, high cost of some electrolytes and most importantly the existence of a smaller number of active electro-active sites. It is seen that MTMO NPs draw huge attention for SCs as they have unique structural features, high stability, variable oxidation states, and can undergo innovative morphological modifications for higher surface area. Due to their better interaction with the electrolyte, MTMOs provide excellent charge storage behavior with the help of large active sites and shorter ion transfer resistance. Flexible SCs based on MTMOs have high conductivity and plenty of active sites and play a significant role in achieving wearable real-life application devices.

Despite these encouraging results, purposeful design and facile, large-scale, and cost-effective fabrication of MTMOs with superior EES performance still remain a challenge. Moreover, in-depth studies on the relationship between the structure/composition/morphology and the EES properties of these MTMOs have not yet been systematically achieved. Despite these challenges, it is found that the discussed metal oxide spinels have great potential for future SC applications and energy-storage devices.

Conflicts of interest

The author declares no conflict of interest.

Acknowledgements

References

1 M. Pumera, *Energy Environ. Sci.*, 2011, **4**, 668–674.

2 M. Winter and R. J. Brodd, *Chem. Rev.*, 2004, **104**, 4245–4270.

3 P. Simon and Y. Gogotsi, *Nat. Mater.*, 2008, **7**, 845–854.

4 D. P. Dubal, O. Ayyad, V. Ruiz and P. Gómez-Romero, *Chem. Soc. Rev.*, 2015, **44**, 1777–1790.

5 Z. Meng, W. Yan, M. Zou, H. Miao, F. Ma, A. B. Patil, R. Yu, X. Y. Liu and N. Lin, *J. Colloid Interface Sci.*, 2021, **583**, 722–733.

6 A. González, E. Goikolea, J. A. Barrena and R. Mysyk, *Renewable Sustainable Energy Rev.*, 2016, **58**, 1189–1206.

7 T. Pettong, P. Iamprasertkun, A. Krittayavathananon, P. Sukha, P. Sirisinudomkit, A. Seubsai, M. Chareonpanich, P. Kongkachuichay, J. Limtrakul and M. Sawangphruk, *ACS Appl. Mater. Interfaces*, 2016, **8**, 34045–34053.

8 W. Zhou, G. Han, Y. Xiao, Y. Chang, W. Yuan, Y. Li, C. Liu and Y. Zhang, *Electrochim. Acta*, 2015, **176**, 594–603.

9 P. Simon, Y. Gogotsi and B. Dunn, *Science*, 2014, **343**, 1210–1211.

10 Y. Gogotsi and R. M. Penner, *ACS Nano*, 2018, **12**, 2081–2083.

11 M. Zhang, Z. Song, H. Liu, A. Wang and S. Shao, *J. Colloid Interface Sci.*, 2021, **584**, 418–428.

12 P. Wu, S. Cheng, M. Yao, L. Yang, Y. Zhu, P. Liu, O. Xing, J. Zhou, M. Wang, H. Luo and M. Liu, *Adv. Funct. Mater.*, 2017, **27**, 1702160.

13 S. Faraji and F. N. Ani, *Renewable Sustainable Energy Rev.*, 2015, **42**, 823–834.

14 T. Das, H. Chauhan, S. Deka, S. Chaudhary, R. Boruah and B. K. Saikia, *Microporous Mesoporous Mater.*, 2017, **253**, 80–90.

15 L. L. Zhang, R. Zhou and X. S. Zhao, *J. Mater. Chem.*, 2010, **20**, 5983–5992.

16 B. De, S. Banerjee, K. D. Verma, T. Pal, P. K. Manna and K. K. Kar, *Handbook of Nanocomposite Supercapacitor Materials II*, 2020, **302**, 179–200.

17 H. Pan, J. Li and Y. P. Feng, *Nanoscale Res. Lett.*, 2010, **5**, 654–668.

18 B. Antil, L. Kumar, K. P. Reddy, C. S. Gopinath and S. Deka, *ACS Sustainable Chem. Eng.*, 2019, **7**, 9428–9438.

19 G. Yang and S. J. Park, *J. Alloys Compd.*, 2018, **741**, 360–367.

20 C. Li, X. Dong, Y. Zhang, J. Hu, W. Liu, X. Cui and A. Hao, *Appl. Surf. Sci.*, 2020, **527**, 146842.

21 N. Wang, P. Zhao, K. Liang, M. Yao, Y. Yang and W. Hu, *Chem. Eng. J.*, 2017, **307**, 105–112.

22 H. Chen, W. Li, M. He, X. Chang, X. Zheng and Z. Ren, *J. Alloys Compd.*, 2021, **855**, 157506.

23 R. Barik and P. P. Ingole, *Curr. Opin. Electrochem.*, 2020, **21**, 327–334.

24 J. Muhommad, L. Kumar, P. K. Baruah, M. R. Das and S. Deka, *Batteries Supercaps*, 2022, **5**, e202100314.

25 R. Chen, L. Liu, J. Zhou, L. Hou and F. Gao, *J. Power Sources*, 2017, **341**, 75–82.

26 S. Trasatti and G. Buzzanca, *J. Electroanal. Chem. Interfacial Electrochem.*, 1971, **29**, A1–A5.

27 W. D. Ryden, A. W. Lawson and C. C. Sartain, *Phys. Rev. B: Solid State*, 1970, **1**, 1494.

28 Y. Shan, M. Y. Zhang, Y. Bai, M. Du, X. Guo and H. Pang, *Chem. Eng. J.*, 2022, **429**, 132146.

29 C. Yang, R. Gao and H. Yang, *EnergyChem*, 2021, **3**, 100062.

30 B. E. Conway, *Electrochemical Supercapacitors: Scientific Fundamentals and Technological Applications*, Springer Science & Business Media, Springer, Boston, MA, 2013, pp. 259–297.

31 C. An, Y. Zhang, H. Guo and Y. Wang, *Nanoscale Adv.*, 2019, **1**, 4644–4658.

32 M. Chauhan, K. P. Reddy, C. S. Gopinath and S. Deka, *ACS Catal.*, 2017, **7**, 5871–5879.

33 M. Chauhan and S. Deka, *ACS Appl. Energy Mater.*, 2019, **3**, 977–986.

34 S. Deka and P. A. Joy, *J. Mater. Chem.*, 2007, **17**, 453–456.

35 G. Pilania, V. Kocevski, J. A. Valdez, C. R. Kreller and B. P. Uberuaga, *Commun. Mater.*, 2020, **1**, 84.

36 Z. Wu, Y. Zhu and X. Ji, *J. Mater. Chem. A*, 2014, **2**, 14759–14772.

37 S. Deka and P. A. Joy, *J. Nanosci. Nanotechnol.*, 2008, **8**, 3955–3958.

38 W. Chen, R. B. Rakhi, L. Hu, X. Xie, Y. Cui and H. N. Alshareef, *Nano Lett.*, 2011, **11**, 5165–5172.

39 S. Adhikari, S. Selvaraj, S. H. Ji and D. H. Kim, *Small*, 2020, **16**, 2005414.

40 K. Deori and S. Deka, *CrystEngComm*, 2013, **15**, 8465–8474.

41 X. H. Xia, J. P. Tu, Y. J. Mai, X. Wang, C. D. Gu and X. B. Zhao, *J. Mater. Chem.*, 2011, **21**, 9319–9326.

42 X. H. Xia, J. P. Tu, Y. Q. Zhang, Y. J. Mai, X. L. Wang, C. D. Gu and X. B. Zhao, *RSC Adv.*, 2012, **2**, 1835–1841.

43 W. Du, R. Liu, Y. Jiang, Q. Lu, Y. Fan and F. Gao, *J. Power Sources*, 2013, **227**, 101–105.

44 C. Zhao, B. Huang, W. Fu, J. Chen, J. Zhou and E. Xie, *Electrochim. Acta*, 2015, **178**, 555–563.

45 X. Fan, Y. Sun, P. Ohlckers and X. Chen, *Appl. Sci.*, 2019, **9**, 4672.

46 M. Wang, J. Zhang, X. Yi, B. Liu, X. Zhao and X. Liu, *Beilstein J. Nanotechnol.*, 2020, **11**, 240–251.

47 R. P. Raj, P. Ragupathy and S. Mohan, *J. Mater. Chem. A*, 2015, **3**, 24338–24348.

48 M. R. Pallavolu, N. Gaddam, A. N. Banerjee, R. R. Nallapureddy, Y. A. Kumar and S. W. Joo, *Electrochim. Acta*, 2022, **407**, 139868.

49 R. K. Nare, S. Ramesh, P. K. Basavi, V. Kakani, C. Bathula, H. M. Yadav, P. B. Dhanapal, R. K. R. Kotanka and V. R. Pasupuleti, *Sci. Rep.*, 2022, **12**, 1998.

50 J. Yesuraj, H. O. Lee, M. K. Pandiyan, J. Jayavelu, M. Bhagavathiachari and K. Kim, *J. Mol. Struct.*, 2022, **1256**, 132499.

51 C. Jiang, M. Yao, Z. Wang, J. Li, Z. Sun, L. Li, K. S. Moon and C. P. Wong, *Carbon*, 2021, **184**, 386–399.

52 K. Deori, S. K. Ujjain, R. K. Sharma and S. Deka, *ACS Appl. Mater. Interfaces*, 2013, **5**, 10665–10672.

53 T. Geng, L. Zhang, H. Wang, K. Zhang and X. Zhou, *Bull. Mater. Sci.*, 2015, **38**, 1171–1175.

54 T. Arun, T. K. Kumar, R. Udayabhaskar, R. V. Mangalaraja and A. A. Fakhrabadi, *Mater. Res. Express*, 2019, **6**, 0850b1.

55 A. T. E. Vilian, B. Dinesh, M. Rethinasabapathy, S.-K. Hwang, C.-S. Jin, Y. S. Huh and Y.-K. Han, *J. Mater. Chem. A*, 2018, **6**, 14367–14379.

56 S. Zheng, Q. Li, H. Xue, H. Pang and Q. Xu, *Natl. Sci. Rev.*, 2020, **7**, 305–314.

57 M. M. Vadiyar, S. S. Kolekar, J.-Y. Chang, A. A. Kashale and A. V. Ghule, *Electrochim. Acta*, 2016, **222**, 1604–1615.

58 H. Zhang, B. Yan, C. Zhou, J. Wang, H. Duan, D. Zhang and H. Zhao, *Energy Fuels*, 2021, **35**, 16925–16932.

59 F. Wu, F. Cui, Q. Ma, J. Zhang, X. Qi and T. Cui, *Mater. Lett.*, 2022, **324**, 132791.

60 S. Zallouz, B. Réty, L. Vidal, J.-M. L. Meins and C. M. Ghimbeu, *ACS Appl. Nano Mater.*, 2021, **4**, 5022–5037.

61 S. A. Beknalkar, A. M. Teli, T. S. Bhat, K. K. Pawar, S. S. Patil, N. S. Harale, J. C. Shin and P. S. Patil, *J. Mater. Sci. Technol.*, 2022, **130**, 227–248.

62 M. Aghazadeh, M. Asadi, M. R. Ganjali, P. Norouzi, B. Sabour and M. Emamal-izadeh, *Thin Solid Films*, 2017, **634**, 24–32.

63 R. Cheraghali and M. Aghazadeh, *Anal. Bioanal. Electrochem.*, 2016, **8**, 193–206.

64 D. Shaik, P. Rosaiah, K. S. Ganesh, Y. Qiu and O. M. Hussain, *Mater. Sci. Semicond. Process.*, 2018, **84**, 83–90.

65 M. S. Ata, J. Milne and I. Zhitomirsky, *J. Colloid Interface Sci.*, 2018, **512**, 758–766.

66 S. Kulkarni, D. Puthusseri, S. Thakur, A. Banpurkar and S. Patil, *Electrochim. Acta*, 2017, **231**, 460–467.

67 H. Pang, J. Deng, J. Du, S. Li, J. Li, Y. Ma, J. Zhang and J. Chen, *Dalton Trans.*, 2012, **41**, 10175–10181.

68 T. Jiang, S. Yang, Z. Bai, P. Dai, X. Yu, M. Wu and H. Hu, *Nanotechnology*, 2018, **29**, 315402.

69 H. Chen, C. Xue, D. Cui, Y. Li, Y. Wang and W. Zhang, *Int. J. Electrochem. Sci.*, 2020, **15**, 966–976.

70 Y. Gao, S. Chen, D. Cao, G. Wang and J. Yin, *J. Power Sources*, 2010, **195**, 1757–1760.

71 D. T. Dam and J. M. Lee, *ACS Appl. Mater. Interfaces*, 2014, **6**, 20729–20737.

72 E. A. A. Aboelazm, G. A. m. Ali, H. Algarni, H. Yin, Y. U. Zhong and K. F. Chong, *J. Phys. Chem. C*, 2018, **122**, 12200–12206.

73 T. Y. Wei, C. H. Chen, K. H. Chang, S. Y. Lu and C. C. Hu, *Chem. Mater.*, 2009, **21**, 3228–3233.

74 T. H. Nguyen, V. H. Nguyen, R. K. Deivasigamani, D. Kharismadewi, Y. Iwai and J. J. Shim, *Solid State Sci.*, 2016, **53**, 71–77.

75 X. Wang, A. Sumboja, E. Khoo, C. Yan and P. S. Lee, *J. Phys. Chem. C*, 2012, **116**, 4930–4935.

76 C. Yuan, L. Yang, L. Hou, L. Shen, F. Zhang, D. Li and X. Zhang, *J. Mater. Chem.*, 2011, **21**, 18183.

77 S. K. Meher and G. R. Rao, *J. Phys. Chem. C*, 2011, **115**, 15646–15654.

78 R. Madhu, V. Veeramani, S. M. Chen, A. Manikandan, A. Y. Lo and Y. L. Chueh, *ACS Appl. Mater. Interfaces*, 2015, **7**, 15812–15820.

79 L. Xiao, H. Qi, K. Qu, C. Shi, Y. Cheng, Z. Sun, B. Yuan, Z. Huang, D. Pan and Z. Guo, *Adv. Compos. Hybrid Mater.*, 2021, **4**, 306–316.

80 S. Liu, L. Kang, J. Hu, E. Jung, J. Zhang, S. C. Jun and Y. Yamauchi, *ACS Energy Lett.*, 2021, **6**, 3011–3019.

81 B. Li, X. Zhang, J. Dou and C. Hu, *Ceram. Int.*, 2019, **45**, 16297–16304.

82 T. Xiong, W. S. V. Lee, X. Huang and J. M. Xue, *J. Mater. Chem. A*, 2017, **5**, 12762–12768.

83 A. G. Naiknaware, J. U. Chavan, S. H. Kaldate and A. A. Yadav, *J. Alloys Compd.*, 2019, **774**, 787–794.

84 J. Yesuraj, S. Vajravijayan, R. Yang, N. Nandhagopal, K. Gunasekaran, N. C. S. Selvam, P. J. Yoo and K. Kim, *Langmuir*, 2022, **38**, 2928–2941.

85 B. Rezaei, T. W. Hansen and S. S. Keller, *ACS Appl. Nano Mater.*, 2021, **5**, 1808–1819.

86 D. P. M. D. Shaik, R. Pitcheri, Y. Qiu and O. M. Hussain, *Ceram. Int.*, 2019, **45**, 2226–2233.

87 S. A. Beknalkar, A. M. Teli, N. S. Harale, K. K. Pawar, D. S. Patil, J. C. Shin and P. S. Patil, *Ceram. Int.*, 2021, **47**, 29771–29785.

88 G. Arrabito, A. Bonasera, G. Prestopino, A. Orsini, A. Mattoccia, E. Martinelli, B. Pignataro and P. G. Medaglia, *Crystals*, 2019, **9**, 361.

89 S. Angelov, E. Zhecheva, K. Petrov and D. Menandjiev, *Mater. Res. Bull.*, 1982, **17**, 235–240.

90 Y. H. Hou, Y. J. Zhao, Z. W. Liu, H. Y. Yu, X. C. Zhong, W. Q. Qiu, D. C. Zeng and L. S. Wen, *J. Phys. D: Appl. Phys.*, 2010, **43**, 445003.

91 L. Kumar, P. K. Boruah, S. Borthakur, L. Saikia, M. R. Das and S. Deka, *ACS Appl. Nano Mater.*, 2021, **4**, 5250–5262.

92 J. Sun, C. Xu and H. Chen, *J. Materiomics*, 2021, **7**, 98–126.

93 A. K. Das, N. H. Kim, S. H. Lee, Y. Sohn and J. H. Lee, *Composites, Part B*, 2018, **150**, 269–276.

94 G. Li, S. Liu, Y. Pan, T. Zhou, J. Ding, Y. Sun and Y. Wang, *J. Alloys Compd.*, 2019, **787**, 694–699.

95 S. K. Kaverlavani, S. E. Moosavifard and A. Bakouei, *J. Mater. Chem. A*, 2017, **5**, 14301–14309.

96 J. Sun, C. Xu and H. Chen, *J. Materiomics*, 2021, **7**, 98–126.

97 Q. Wang, D. Chen and D. Zhang, *RSC Adv.*, 2015, **5**, 96448–96454.

98 B. S. Singu, R. Kuchi, P. C. Van, D. Kim, K. R. Yoon and J. R. Jeong, *ChemNanoMat*, 2019, **5**, 1398–1407.

99 S. Vijayakumar, S. H. Lee and K. S. Ryu, *Electrochim. Acta*, 2015, **182**, 979–986.

100 A. A. Ensafi, S. E. Moosavifard, B. Rezaei and S. K. Kaverlavani, *J. Mater. Chem. A*, 2018, **6**, 10497–10506.

101 S. K. Kaverlavani, S. E. Moosavifard and A. Bakouei, *Chem. Commun.*, 2017, **53**, 1052–1055.

102 A. Pendashteh, M. S. Rahmanifar, R. B. Kaner and M. F. Mousavi, *Chem. Commun.*, 2014, **50**, 1972.

103 H. Chen, X. Chen, Y. Zeng, S. Chen and J. Wang, *RSC Adv.*, 2015, **5**, 70494–70497.

104 S. Liu, D. Ni, H. F. Li, K. N. Hui, C. Y. Ouyang and S. C. Jun, *J. Mater. Chem. A*, 2018, **6**, 10674–10685.

105 Y. Gai, Y. Shang, L. Gong, L. Su, L. Hao, F. Dong and J. Li, *RSC Adv.*, 2017, **7**, 1038–1044.

106 Z. Gao, L. Zhang, J. Chang, Z. Wang, D. Wu, F. Xu, Y. Guo and K. Jiang, *Appl. Surf. Sci.*, 2018, **442**, 138–147.

107 H. Chen, Q. Zhang, J. Wang, Q. Wang, X. Zhou, X. Li, Y. Yang and K. Zhang, *Nano Energy*, 2014, **10**, 245–258.

108 J. Eum, D. Mandal and H. Kim, *J. Electroanal. Chem.*, 2021, **892**, 115299.

109 B. Guan, D. Guo, L. Hu, G. Zhang, T. Fu, W. Ren, J. Li and Q. Li, *J. Mater. Chem. A*, 2014, **2**, 16116–16123.

110 W. Bai, H. Tong, Z. Gao, S. Yue, S. Xing, S. Dong, L. Shen, J. He, X. Zhang and Y. Liang, *J. Mater. Chem. A*, 2015, **3**, 21891–21898.

111 B. Liu, B. Liu, Q. Wang, X. Wang, Q. Xiang, D. Chen and G. Shen, *ACS Appl. Mater. Interfaces*, 2013, **5**, 10011–10017.

112 K. Qiu, Y. Lu, D. Zhang, J. Cheng, H. Yan, J. Xu, X. Liu, J. K. Kim and Y. Luo, *Nano Energy*, 2015, **11**, 687–696.

113 C. Wu, J. Cai, Q. Zhang, X. Zhou, Y. Zhu, L. Li, P. Shen and K. Zhang, *Electrochim. Acta*, 2015, **169**, 202–209.

114 S. Raut and B. Sankapal, *J. Colloid Interface Sci.*, 2017, **487**, 201–208.

115 S. Vijayakumar, S. Nagamuthu, S. H. Lee and K. S. Ryu, *Int. J. Hydrogen Energy*, 2017, **42**, 3122–3129.

116 Y. Pan, H. Gao, M. Zhang, L. Li and Z. Wang, *J. Alloys Compd.*, 2017, **702**, 381–387.

117 D. Song, J. Zhu, J. Li, T. Pu, B. Huang, C. Zhao, L. Xie and L. Chen, *Electrochim. Acta*, 2017, **257**, 455–464.

118 Z. Gao, L. Zhang, J. Chang, Z. Wang, D. Wu, F. Xu, Y. Guo and K. Jiang, *Appl. Surf. Sci.*, 2018, **442**, 138–147.

119 Y. Jiang, L. Chen, H. Zhang, Q. Zhang, W. Chen, J. Zhu and D. Song, *Chem. Eng. J.*, 2016, **292**, 1–12.

120 M. U. A. Prathap and R. Srivastava, *Nano Energy*, 2013, **2**, 1046–1053.

121 T. Y. Wei, C. H. Chen, H. C. Chien, S. Y. Lu and C. C. Hu, *Adv. Mater.*, 2010, **22**, 347–351.

122 S. Liu, L. Hu, X. Xu, A. A. Al-Ghamdi and X. Fang, *Small*, 2015, **11**, 4267–4283.

123 L. Pang and H. Wang, *Adv. Mater. Technol.*, 2021, 2100501.

124 L. Kumar, H. Chauhan, N. Yadav, N. Yadav, S. A. Hashmi and S. Deka, *ACS Appl. Energy Mater.*, 2018, **1**, 6999–7006.

125 L. Kumar, P. K. Boruah, M. R. Das and S. Deka, *ACS Appl. Mater. Interfaces*, 2019, **11**, 37665–37674.

126 L. Kumar, M. Chauhan, P. K. Boruah, M. R. Das, S. A. Hashmi and S. Deka, *ACS Appl. Energy Mater.*, 2020, **3**, 6793–6804.

127 H. Hu, B. Guan, B. Xia and X. W. Lou, *J. Am. Chem. Soc.*, 2015, **137**, 5590–5595.

128 T. Zhu, H. Zhang, Y. Sha, Y. Huang, Y. Li, D. Zhao and X. Gao, *Z. Anorg. Allg. Chem.*, 2020, **646**, 53–57.

129 C. Pan, Z. Liu, W. Li, Y. Zhuang, Q. Wang and S. Chen, *J. Phys. Chem. C*, 2019, **123**, 25549–25558.

130 M. K. Paliwal and S. K. Meher, *ACS Appl. Nano Mater.*, 2020, **3**, 4241–4252.

131 S. Dou, P. Li, D. Tan, H. Li, L. Ren and F. Wei, *Energy*, 2021, **227**, 120540.

132 B. Xue, Y. Guo, Z. Huang, S. Gu, Q. Zhou, W. Yang and K. Li, *Dalton Trans.*, 2021, **50**, 9088–9102.

133 T. Kavinkumar, N. Naresh, G. Mathew and B. Neppolian, *J. Alloys Compd.*, 2022, **891**, 162052.

134 Y. Zhang, Y. Xue, R. Yang, K. Zhang, A. Qin and S. Chen, *J. Alloys Compd.*, 2022, **898**, 162791.

135 S. Wang, P. Yang, X. Sun, L. Feng, C. Jin, M. Ren, H. Xing and J. Shi, *J. Phys. Chem. Solids*, 2021, **159**, 110257.

136 A. Chowdhury, S. Biswas, V. Sharma, J. Halder, A. Dhar, B. Sundaram, B. Dubey, P. S. Burada and A. Chandra, *Electrochim. Acta*, 2021, **397**, 139252.

137 M. Kandasamy, S. Sahoo, S. K. Nayak, B. Chakraborty and C. S. Rout, *J. Mater. Chem. A*, 2021, **9**, 17643–17700.

138 J. Sun, X. Du, R. Wu, Y. Zhang, C. Xu and H. Chen, *ACS Appl. Energy Mater.*, 2020, **3**, 8026–8037.

139 M. Sun, Q. Fang, Z. Li, C. Cai, H. Li, B. Cao, W. Shen, T. X. Liu and Y. Fu, *Electrochim. Acta*, 2021, **397**, 139306.

140 J. Sun, X. Tian, C. Xu and H. Chen, *J. Materiomics*, 2021, **7**, 1358–1368.

141 D. Liu, Y. Liu, X. Liu, C. Xu, J. Zhu and H. Chen, *J. Energy Storage*, 2022, **52**, 105048.

142 A. Pendashteh, S. E. Moosavifard, M. S. Rahmanifar, Y. Wang, M. F. El-Kady, R. B. Kaner and M. F. Mousavi, *Chem. Mater.*, 2015, **27**, 3919–3926.

143 L. Xu, Y. Zhao, J. Lian, Y. Xu, J. Bao, J. Qiu, L. Xu, H. Xu, M. Hua and H. Li, *Energy*, 2017, **123**, 296–304.

144 Y. A. Kumar, K. D. Kumar and H. E. Kim, *Electrochim. Acta*, 2020, **330**, 135261.

145 Y. Shang, T. Xie, C. Ma, L. Su, Y. Gai, J. Liu and L. Gong, *Electrochim. Acta*, 2018, **286**, 103–113.

146 Y. Lu, L. Wang, M. Chen, Y. Wu, G. Liu, P. Qi, M. Fu, H. Wu and Y. Tang, *J. Alloys Compd.*, 2021, **876**, 160037.

147 G. P. Kamble, A. S. Rasal, S. B. Gaikwad, V. S. Gurav, J. Y. Chang, S. S. Kolekar, Y. C. Ling and A. V. Ghule, *ACS Appl. Nano Mater.*, 2021, **4**, 12702–12711.

148 J. Bhagwan, G. Nagaraju, B. Ramulu, S. C. Sekhar and J. Yu, *Electrochim. Acta*, 2019, **299**, 509–517.

149 W. Luo and H. Xue, *Fullerenes, Nanotubes, Carbon Nanostruct.*, 2018, **27**, 189–197.

150 H. Fu, Y. Liu, L. Chen, Y. Shi, W. Kong, J. Hou, F. Yu, T. Wei, H. Wang and X. Guo, *Electrochim. Acta*, 2019, **296**, 719–729.

151 H. Gao, Y. Cao, Y. Chen, Z. Liu, M. Guo, S. Ding, J. Tu and J. Qi, *Appl. Surf. Sci.*, 2019, **465**, 929–936.

152 M. Sethi and D. K. Bhat, *J. Alloys Compd.*, 2019, **781**, 1013–1020.

153 W. Li, F. Yang, Z. Hu and Y. Liu, *J. Alloys Compd.*, 2018, **749**, 305–312.

154 W. Zhang, W. Xin, T. Hu, Q. Gong, T. Gao and G. Zhou, *Ceram. Int.*, 2019, **45**, 8406–8413.

155 J. Nan, Y. Shi, Z. Xiang, S. Wang, J. Yang and B. Zhang, *Electrochim. Acta*, 2019, **301**, 107–116.

156 D. R. Kumar, K. R. Prakasha, A. S. Prakash and J. J. Shim, *J. Alloys Compd.*, 2020, **836**, 155370.

157 F. Yang, K. Zhang, W. Li and K. Xu, *J. Colloid Interface Sci.*, 2019, **556**, 386–391.

158 W. Chu, Z. Shi, Y. Hou, D. Ma, X. Bai, Y. Gao and N. Yang, *ACS Appl. Mater. Interfaces*, 2019, **12**, 2763–2772.

159 M. V. Kiamahalleh, S. H. S. Zein, G. Najafpour, S. A. Sata and S. Buniran, *Nano*, 2012, **7**, 1230002.

160 C. Zhong, Y. Deng, W. Hu, D. Sun, X. Han, J. Qiao and J. Zhang, *Electrolytes for electrochemical supercapacitors*, CRC Press, Boca Raton, 2016.

161 C. Zhong, Y. Deng, W. Hu, J. Qiao, L. Zhang and J. Zhang, *Chem. Soc. Rev.*, 2015, **44**, 7484–7539.

162 L. Zhou, C. Li, X. Liu, Y. Zhu, Y. Wu and T. Ree, Metal oxides in supercapacitors, in *Metal oxides: Metal Oxides in Energy Technologies*, ed. Y. Wu, Elsevier, 2018, pp. 169–203.

163 B. Pal, S. Yang, S. Ramesh, V. Thangadurai and R. Jose, *Nanoscale Adv.*, 2019, **1**, 3807–3835.

164 C. Zhong, Y. Deng, W. Hu, J. Qiao, L. Zhang and J. Zhang, *Chem. Soc. Rev.*, 2015, **44**, 7484–7539.

165 E. Frackowiak, M. Meller, J. Menzel, D. Gastol and K. Fic, *Faraday Discuss.*, 2014, **172**, 179–198.

166 S. Shahzad, A. Shah, E. Kowsari, F. J. Iftikhar, A. Nawab, B. Piro, M. S. Akhter, U. A. Rana and Y. Zou, *Global Challenges*, 2018, **3**, 1800023.

167 B. E. Francisco, C. M. Jones, S.-H. Lee and C. R. Stoldt, *Appl. Phys. Lett.*, 2012, **100**, 103902.

168 M. A. A. M. Abdah, N. H. N. Azman, S. Kulandaivalu and Y. Sulaiman, *Mater. Des.*, 2020, **186**, 108199.

169 C. Lamiel, Y. R. Lee, M. H. Cho, D. Tuma and J.-J. Shim, *J. Colloid Interface Sci.*, 2017, **507**, 300–309.

170 D. P. Dubal, P. Gomez-Romero, B. R. Sankapal and R. Holze, *Nano Energy*, 2015, **11**, 377–399.

171 S. Palchoudhury, K. Ramasamy, R. K. Gupta and A. Gupta, *Front. Mater.*, 2019, **5**, 83.

172 L. Huang, D. Chen, Y. Ding, S. Feng, Z. Wang and M. Liu, *Nano Lett.*, 2013, **13**, 3135–3139.

173 G. Zhang and X. W. (David) Lou, *Sci. Rep.*, 2013, **3**, 1470.

174 J. Du, G. Zhou, H. Zhang, C. Cheng, J. Ma, W. Wei, L. Chen and T. Wang, *ACS Appl. Mater. Interfaces*, 2013, **5**, 7405–7409.

175 R. K. Gupta, J. Candler, S. Palchoudhury, K. Ramasamy and B. K. Gupta, *Sci. Rep.*, 2015, **5**, 15265.

176 Y. Zheng, Z. Lin, W. Chen, B. Liang, H. Du, R. Yang, X. He, Z. Tang and X. Gui, *J. Mater. Chem. A*, 2017, **5**, 5886–5894.

177 S. Chai, K. Dong, T. Wu and Q. Wu, *ChemElectroChem*, 2021, **8**, 3894–3903.

178 Q. Wang, X. Wang, J. Xu, X. Ouyang, X. Hou, D. Chen, R. Wang and G. Shen, *Nano Energy*, 2014, **8**, 44–51.

179 Z. Y. Yu, L. F. Chen and S. H. Yu, *J. Mater. Chem.*, 2014, **2**, 10889.

180 Z.-Y. Yu, L.-F. Chen and S.-H. Yu, *J. Mater. Chem. A*, 2014, **2**, 10889–10894.

181 S. B. Bandgar, M. M. Vadiyar, Y.-C. Ling, J.-Y. Chang, S.-H. Han, A. V. Ghule and S. S. Kolekar, *ACS Appl. Energy Mater.*, 2018, **1**, 638–648.

182 M. M. Vadiyar, S. C. Bhise, S. S. Kolekar, J.-Y. Chang, K. S. Ghule and A. V. Ghule, *J. Mater. Chem. A*, 2016, **4**, 3504–3512.

183 X. Liang, Q. Wang, Y. Ma and D. Zhang, *Dalton Trans.*, 2018, **47**, 17146–17152.

184 G. Wei, X. Zhao, K. Du, Y. Huang, C. An, S. Qiu, M. Liu, S. Yao and Y. Wu, *Electrochim. Acta*, 2018, **283**, 248–259.

185 Q. Wang, J. Xu, X. Wang, B. Liu, X. Hou, G. Yu, P. Wang, D. Chen and G. Shen, *ChemElectroChem*, 2014, **1**, 559–564.

186 M. Kuang, X. Y. Liu, F. Dong and Y. X. Zhang, *J. Mater. Chem. A*, 2015, **3**, 21528–21536.

187 D. Zhu, X. Sun, J. Yu, Q. Liu, J. Liu, R. Chen, H. Zhang, R. Li, J. Yu and J. Wang, *J. Colloid Interface Sci.*, 2019, **557**, 76–83.

188 A. Basu, M. Bhardwaj, Y. Gawli, C. Rode and S. Ogale, *ChemistrySelect*, 2016, **1**, 5159.

189 H. Wu, Z. Lou, H. Yanga and G. Shen, *Nanoscale*, 2015, **7**, 1921–1926.

190 J. Zhao, C. Li, Q. Zhang, J. Zhang, X. Wang, Z. Lin, J. Wang, W. Lv, C. Lu, C.-p. Wong and Y. Yao, *J. Mater. Chem. A*, 2017, **5**, 6928–6936.